# A numerical investigation of tsunamis impacting dams

Tommaso Attili[a], Valentin Heller[a], Savvas Triantafyllou[b]

[a]*Environmental Fluid Mechanics and Geoprocesses Research Group, Faculty of Engineering, University of Nottingham, Nottingham NG7 2RD, UK*
[b]*Institute for Structural Analysis and Aseismic Research, School of Civil Engineering, National Technical University of Athens, Athens, Greece*

**Abstract**

Landslides, rockfalls, and iceberg calving impacting into a water body generate large landslide-tsunamis posing a serious hazard in lakes and reservoirs. These waves can impact and even overtop dams as in the 1963 Vajont disaster in Italy. However, estimating the effects of tsunamis on dams, e.g. pressures and forces, and 3D effects is challenging. An accurate prediction of these effects is also important for a range of coastal and offshore applications. The present study focuses on the numerical modelling of landslide-tsunamis impacting dams with the open source toolbox solids4foam. After a validation with theoretical, experimental, and numerical results, 5th order Stokes, cnoidal, and solitary waves were simulated in 72 2D experiments with dams of steep to vertical inclinations. The wave loading on dams was found to be in agreement with predictions based on an existing empirical approach, significantly expanding its limited validation conditions. New empirical equations are suggested to predict the wave run-up height together with the overtopping volume and depth. These address the cases where no empirical equations are available or existing equations result in large deviations from the numerical results. Novel insight in the dynamic pressure is provided, supported by new semi-empirical equations. Further, simulations in 3D were performed to quantify the effects of the dam curvature and asymmetrical wave impact angles. Both effects combined induce an increase in the run-up height at dam flanks of up to 32%. Such findings support the design of dams and tsunami hazard assessment.

*Email addresses:* `tommaso.attili@nottingham.ac.uk` (Tommaso Attili), `valentin.heller@nottingham.ac.uk` (Valentin Heller), `savtri@mail.ntua.gr` (Savvas Triantafyllou)

*Keywords:* Impulse waves, Landslide-tsunamis, Numerical modelling, Tsunamis, Wave-structure interaction.

---

# 1. Introduction

## *1.1. Background*

Landslide-tsunamis, also called landslide-generated impulse waves, are generated by landslides, rockfalls, and iceberg calving in water bodies such as lakes and reservoirs (Heller and Hager, 2010; Heller et al., 2016; Bullard et al., 2019; Evers et al., 2019; Meng et al., 2020; Heller et al., 2021; Rauter et al., 2021; Ruffini et al., 2021). The energies of such gravity-driven masses are transferred into waves propagating across water bodies and potentially interacting with dams. This may result in significant run-ups and even overtoppings (Kobel et al., 2017; Evers and Boes, 2019; Evers et al., 2019). Several destructive landslide-tsunamis have been documented in the recent past. Among these, the one generated in the Vajont reservoir in Italy, in 1963, caused approximately 2000 casualties (Panizzo et al., 2005b). More recently, the 2014 Lake Askja event on Iceland resulted in a run-up height of 71 m (Gylfadóttir et al., 2017). Such events represent a persistent danger in regions with a large number of lakes, fjords, and/or reservoirs such as China and Norway.

Studies into the risk of tsunamis must be carried out for large water bodies (Swiss Federal Office of Energy, 2015), including tsunami impact and dam overtopping. In addition to the hydrostatic force from the still water, tsunami forces may be relevant (Ramsden, 1996) and an accurate prediction is important for the design of dams and a range of further coastal and offshore structures, e.g. oil and gas rigs, offshore wind turbine platforms, breakwaters, flood protection systems, and wave energy converters. Nevertheless, the estimation of tsunami forces is still associated with large uncertainties. Available prediction methods are based on a small number of 2D laboratory experiments (Ramsden, 1996). Moreover, 3D effects, e.g. the dam curvature and/or asymmetrical wave impact angles, often have to be neglected due to a lack of knowledge (Heller et al., 2009). Wave run-ups are also important for the design of dams, e.g. to prevent dam overtoppings. This may cause severe damage to the dam, e.g. at the crest or downstream slope, and/or to the downstream area.

The present study focuses on the numerical investigation of tsunamis impacting dams to enhance hazard assessment. Tsunamis are modelled with idealised wave types representing a wide range of impulse waves, e.g. generated by earthquakes, landslides, and icebergs. Computational fluid dynamics (CFD) shows a great potential in modelling tsunamis (Yavari-Ramshe and Ataie-Ashtiani, 2016), waves impacting walls (He and Kashiwagi, 2012; Chen et al., 2014; Didier et al., 2014; Hu et al., 2016), and impulsive wave forces acting on recurved parapets (Castellino et al., 2018; Martinelli et al., 2018; Castellino et al., 2021; Dermentzoglou et al., 2021). Mesh-based methods, e.g. the Finite Volume Method (FVM, Tuković et al., 2018), and mesh-free methods (particle-based), e.g. Smoothed Particle Hydrodynamics (SPH, Didier et al., 2014), have been successfully applied. However, mesh-based methods are more computationally efficient and demonstrate a good convergence behaviour (Yavari-Ramshe and Ataie-Ashtiani, 2016).

Recently, new approaches have been developed for modelling waves generated by rigid bodies such as landslides. Chen et al. (2020) and Romano et al. (2020) presented new methods based on the Immersed Boundary Method and Overset Mesh Technique, respectively, in the OpenFOAM framework. Lagrangian approaches, e.g. the Particle Finite Element Method, have also been applied as they are efficient in solving large deformations (Franci et al., 2020; Mulligan et al., 2020). Furthermore, a new multi-domain method was developed by Di Paolo et al. (2021) to simulate wave-structure interactions in OpenFOAM. The present study relies on an available FVM toolbox in foam-extend 4.0 (FE 4.0), capable of simulating both the fluid and structure.

### *1.2. Previous work*

An accurate prediction of the effects of tsunamis on dams is still challenging. The total pressure $p$ at the dam is composed of the dynamic $p_d$ and hydrostatic components. An analytical formulation of $p_d$ for linear waves propagating offshore in a water body was developed by Dean and Dalrymple (1991) (Section 3.2.3). Sainflou (1928) derived an analytical solution for $p_d$ from nonlinear and standing waves on a vertical wall. Tadjbakhsh and Keller (1960) provided the theoretical $p_d$ and water surface elevation $\eta$ in function of the time $t$ and the spatial coordinate $x$ for periodic waves impacting a vertical wall. As the methods of Sainflou (1928) and Tadjbakhsh and Keller (1960) were originally developed for wind waves, they may be inappropriate to predict wave pressures for more extreme cases, such as tsunamis.

Landslide-tsunamis can be approximated with Stokes (Dean and Dalrymple, 1991), cnoidal (Dingemans, 1997), solitary (Boussinesq, 1871), and bore (Le Méhauté, 1976) waves (Heller and Hager, 2011; Heller and Spinneken, 2015; Xue et al., 2019). These different wave types result in different effects when impacting dams. Bore-like waves are typically created in the generation zone and transform into cnoidal- or solitary-like waves further offshore (Heller and Hager, 2011) or they are generated during wave breaking near the shore. Wave breaking rarely occurs at a dam as the water depth tends to increase and the wave amplitude tends to decrease towards the dam; hence, solitary-like waves represent the most extreme case in most situations (Heller et al., 2009; Kobel et al., 2017).

A mathematical investigation of solitary waves impacting a vertical wall was conducted by Cooker et al. (1997). The numerically deduced values of the wave force and the run-up height $R$ were successfully validated with the numerical results of Fenton and Rienecker (1982). However, no prediction method for the pressure distribution at the wall was provided.

Ramsden (1996) conducted laboratory experiments in a 0.610 m (height) $\times$ 0.396 m (width) $\times$ 36.6 m (length) wave tank to investigate the effects of solitary waves on a vertical wall. The horizontal (subscript $H$) force $F_H$ and bending moment $M_H$ relative to the foundation resulting from the solitary wave and hydrostatic pressure from the still water combined were measured. In an effort to present a coherent methodology to predict the effects of tsunamis in lakes and reservoirs, Heller et al. (2009) approximated the empirical data of Ramsden (1996). They found for a wave amplitude $a$ to water depth $h$ ratio range $0 \leq a/h \leq 0.6$

$$F_H = [1 - 1.5(a/h)]^{1/6}(1/2)\rho_w g(2a + h)^2, \tag{1}$$

$$M_H = [1 - 1.5(a/h)]^{1/6}(1/6)\rho_w g(2a + h)^3 \tag{2}$$

with the water (subscript $w$) density $\rho_w$ and the gravitational acceleration $g$. Eqs. (1) and (2) provide the force and moment per unit width of the dam based on a triangular distribution of the pressure

$$p(z) = [1 - 1.5(a/h)]^{1/6}\rho_w g(2a - z) \tag{3}$$

with a maximum water level of $2a + h$ and $z$ as the vertical coordinate. This is reduced to a trapezoidal distribution in the case of wave overtoppings (Appendix A), i.e. for a dam height $l \leq (2a+h)$, the triangular section above the dam crest is removed (Heller et al., 2009). This results in the reduced (subscript *red*) force $F_{H,red}$ (Eq. A.1) and moment $M_{H,red}$. This approach was taken over by Evers et al. (2019) in their effort to update the manual

Heller et al. (2009). Eqs. (1) and (2) require further validation as they rely on a limited number of experiments and wave conditions.

The most recent prediction methods for $R$ and dam overtopping were summarised by Evers et al. (2019). For $R$, the semi-empirical equation of Evers and Boes (2019) was proposed and for the wave overtopping volume $V\!\!\!\!-$, duration and the maximum wave overtopping depth $d_0$, the methods of Kobel et al. (2017) were recommended. Unfortunately, the empirical equation for $V\!\!\!\!-$ cannot be applied if $a$ is larger than the freeboard $f$, being one of the shortcomings addressed in the present work. These methods will be compared and discussed with the results of the present article in Sections 3 and 4.

### *1.3. Aims and structure*

The present study aims to:

- Provide new physical insight into tsunamis impacting dams of steep to vertical inclinations based on 2D and 3D numerical modelling.
- Provide insight and propose a new semi-empirical approach to predict the dynamic pressure of tsunamis on dams in analogy to the theory of Dean and Dalrymple (1991).
- Expand the validation conditions of the prediction methods of Evers et al. (2019) for tsunami forces on dams with and without overtopping.
- Provide a new empirical equation for the run-up height to support tsunami hazard assessment.
- Provide new empirical equations for the overtopping volume and depth for cases where the equations of Kobel et al. (2017) cannot be applied or result in significantly different predictions from the numerical results.

The remainder of this article is organised as follows. In Section 2 the numerical toolbox is addressed along with the numerical set-ups and the test programme. The validation of the numerical toolbox with laboratory data, an analytical solution and another numerical solver is presented in Section 3. Thereafter, the investigation of tsunami forces, run-ups, overtoppings, and dynamic pressures for waves with and without overtopping in 2D is addressed. A discussion of the results and the 3D simulations can be found in Section 4 followed by the main conclusions in Section 5. The appendices include the overtopping wave force method of Evers et al. (2019) (Appendix A), the convergence tests (Appendix B), and the dynamic pressure (Appendix C) for overtopping waves.

## 2. Methodology

The open source toolbox solids4foam (Cardiff et al., 2018) implemented in FE 4.0 (OpenFOAM extension, 2016) was used in the present study to model tsunamis impacting dams. This toolbox solves fluid-solid interaction problems with a Finite Volume discretisation for both domains and a partitioned coupling approach is applied.

### *2.1. Governing equations of fluid*

The governing equations of an incompressible Newtonian fluid are the continuity and the Reynolds-averaged Navier-Stokes (RANS) equations

$$\nabla \cdot \bar{\mathbf{u}} = 0 \tag{4}$$

$$\frac{\rho \partial \bar{\mathbf{u}}}{\partial t} + \rho(\bar{\mathbf{u}} \cdot \nabla)\bar{\mathbf{u}} = -\nabla \bar{p} + \rho \nabla \cdot (\mu \nabla \cdot \bar{\mathbf{u}} - \overline{\mathbf{u}'\mathbf{u}'}) + \rho \mathbf{g}. \tag{5}$$

In Eqs. (4) and (5) $\bar{\mathbf{u}} = (\bar{u}_x, \bar{u}_y, \bar{u}_z)$ is the mean fluid velocity vector, $\bar{p}$ the mean pressure, $\rho$ the fluid density, $\mu$ the fluid dynamic viscosity, $\overline{\mathbf{u}'\mathbf{u}'}$ the turbulent stress tensor (with $\overline{\mathbf{u}'\mathbf{u}'} = 0$ for laminar flow) and $\mathbf{g}$ the gravitational acceleration vector. Based on the Boussinesq approximation (Jasak, 1996)

$$\overline{\mathbf{u}'\mathbf{u}'} = \nu_t(\nabla \cdot \bar{\mathbf{u}} + (\nabla \cdot \bar{\mathbf{u}})^T) + \frac{2}{3} k_t \mathrm{I}, \tag{6}$$

where I is the identity matrix and $\nu_t$ and $k_t$ are the kinematic turbulent viscosity and the turbulent kinetic energy per unit mass defined by the selected turbulence model in FE 4.0 (Ferziger, 1987). For the simulations of the present study, the laminar flow model has been used (Streeter and Wylie, 1985). This assumption provides accurate results while reducing the associated computational costs, as demonstrated in the validation tests (Section 3.1.1 and 3.1.3), with a tendency to operate on the safe side.

The solver interFoam is applied in FE 4.0 to solve Eqs. (4) and (5). These are discretised into a set of algebraic equations based on the spatial and temporal partition of the domain using the cell-centered FVM and solved with the PIMPLE loop (Aguerre et al., 2013). Time integration is governed by the Courant-Friedrichs-Lewy (CFL) convergence condition (Courant et al., 1928), which is expressed in two dimensions as

$$C = \frac{\bar{u}_x \Delta t}{\Delta x} + \frac{\bar{u}_z \Delta t}{\Delta z} \leq 1. \tag{7}$$

In Eq. (7), $C$ is the Courant number, $\Delta t$ the time step and $\Delta x$ and $\Delta z$ are the cell sizes in the $x$ and $z$ direction, respectively. Once the solver started, the initial $\Delta t$ was continuously adapting to satisfy the CFL condition.

The Volume of Fluid (VOF) method (Hirt and Nichols, 1981) is employed in interFoam to solve water-air flows based on the fraction of volume $\alpha$; $\alpha$ varies from 0 to 1, with $\alpha = 0$ denoting air, $\alpha = 1$ water and $0 < \alpha < 1$ the air-water interface. In the present study, $\alpha = 0.5$ was selected to track the water surface. The fluid properties $\rho$ and $\mu$ are evaluated as

$$\rho = \rho_w \alpha + \rho_a (1 - \alpha) \tag{8}$$

$$\mu = \mu_w \alpha + \mu_a (1 - \alpha) \tag{9}$$

with the subscript $a$ standing for air. Once the fluid velocity field is solved, $\alpha$ is updated through the following transport equation over time

$$\frac{\partial \alpha}{\partial t} + \nabla \cdot (\bar{\mathbf{u}} \alpha) + \nabla \cdot [\alpha (1 - \alpha) \mathbf{u}_r] = 0. \tag{10}$$

The artificial compression term $\nabla \cdot [\alpha(1 - \alpha)\mathbf{u}_r]$, including the compression velocity vector $\mathbf{u}_r$, was introduced by Weller et al. (1998) to reduce the numerical diffusion.

Wave generation was performed with the toolbox waves2Foam (Jacobsen et al., 2012). Several wave theories are implemented in waves2Foam, including linear, Stokes, cnoidal, and solitary wave theory. The governing equations are implemented as in FE 4.0 with the only difference that Eq. (5) is written in terms of the pressure in excess to the hydrostatic one. The wave generation is based on the relaxation zone technique, consisting of a relaxation function applied to evaluate $\bar{\mathbf{u}}$ and $\alpha$ inside the relaxation zone (Jacobsen et al., 2012). In the present study, a relaxation zone of 3 times the wave length $L$ was used in all the 2D tests (Fig. 1a).

### *2.2. Numerical set-up and test programme*

The numerical set-up consisted of a 2D wave channel with a rigid dam (Fig. 1a). The dam with height $l = 50.00$ m and thickness $s = 2.50$ m was located $4L$ from the upstream boundary of the wave flume. Water depths of $h = 25$, 36, and 48 m were used (Table 1), resulting in relative submergences of the dam of $h/l = 0.50$, 0.72, and 0.96 with a minimum freeboard of $f = l - h = 2$ m, satisfying the criterion of the Bureau of Reclamation (2012). The simulations involved a range of wave types impacting dams of inclinations $\beta = 60, 75$, and $90°$. The wave types and corresponding wave features used in the simulations are shown in Table 1 where $H$ is the wave height and $T$ the wave period.

In the cnoidal and Stokes wave tests a resolution of $\Delta x = L/310$ and $\Delta z = 50.00$ cm, with $\Delta x = L/1240$ and $\Delta z = 12.50$ cm in the $L/4 \times 80$ m refined area, was employed. In the solitary wave tests, the domain was discretised with square cells of $\Delta x = \Delta z = 25.00$ cm and a higher resolution of $\Delta x = \Delta z = 6.25$ cm in a 25 m $\times$ 80 m area in front of the dam (Fig. 1a). Finer resolutions were investigated in a few tests, requiring higher computation times without any significant difference in the results (Appendix B.1).

**Table 1**
The test programme for the 2D tests. Values marked with * were observed at $x = -h\cot\beta$ in simulations conducted without the dam and are slightly different, due to bottom friction, from the round values used at the input.

| Parameter | Symbol | Unit | Range | | Dimensionless range |
|---|---|---|---|---|---|
| Water depth | $h$ | m | 25, 36, 48 | - | - |
| Dam height | $l$ | m | 50 | - | - |
| Dam inclination | $\beta$ | ° | 60, 75, 90 | - | - |
| Stokes 5th | $H$ | m | 6.56 to 6.86* | $H/h$ | 0.13 to 0.26 |
| order waves | $T$ | s | 15, 20 | $T(g/h)^{0.5}$ | 6.8 to 12.5 |
| Cnoidal waves | $H$ | m | 5.56 to 6.60* | $H/h$ | 0.13 to 0.26 |
| | $T$ | s | 15 to 30 | $T(g/h)^{0.5}$ | 7.2 to 18.8 |
| Solitary waves | $a$ | m | 2.53 to 15.70* | $a/h$ | 0.10 to 0.60 |

Some initial tests were run with and without solving the governing equations of the solid. The computation times decreased by approximately 60% for the latter cases, and negligible differences ($\approx$ 1 to 2%) were observed in the wave forces on the dam. Consequently, all tests in Table 1 were conducted by solving the fluid governing equations only. The simulations were conducted on the High Performance Computing cluster Augusta at the University of Nottingham using 40 Central Processing Unit (CPU) cores and 120 GB of memory. Stokes and cnoidal wave tests ($\approx 0.4$ million of cells) took approximately 12 h of computation time to simulate 140 to 200 s. A simulation time of 25 s for a solitary wave test ($\approx 1.3$ millions of cells) required approximately 6 h of computation time.

#### *2.2.1. 3D simulations*

In order to provide some insight into the effects of the curvature of the dam and/or asymmetrical wave impact angles, 3D simulations were also conducted. The numerical set-up consisted of a 50 m wide wave tank with a 50 m high dam and $h = 25$ m (Fig. 1). Solitary waves with $a/h = 0.30$ and propagation angles of $\gamma = 0$ and 30° (Fig. 1c,d) impacting gravity and arch dams (Fig. 1a,b) were simulated, resulting in 4 tests. A straight axis was assumed for the gravity dam (Fig. 1a,c) and the upstream face of the arch dam (Fig. 1b,d) was designed with vertical and horizontal radii of 30 and 115 m (Bureau of Reclamation, 2013). The domain was discretised with square cells of $\Delta x = \Delta y = \Delta z = 25.00$ cm and with a higher resolution of $\Delta x = \Delta y = \Delta z = 6.25$ cm in a refined area in front of the dam (Fig. 1a,b).

For $\gamma = 0°$, only half of the domain (0 m $\leq y \leq$ 25 m) was simulated given the symmetry of the wave field ($\approx 40$ million cells). The boundary condition for the plane $y = 0$ m was set as "symmetryPlane" (OpenFOAM documentation, 2020). At $y = 25$ m, the "noSlip" and "zeroGradient" conditions were used for the velocity and pressure fields. These simulations were conducted using 40 CPU cores and 600 GB of memory, requiring approximately 6 days of computation time to simulate 10 s.

For $\gamma = 30°$, the whole domain was used ($\approx 75$ million cells). At $y = -25$ and 25 m, the boundary conditions were set as "noSlip" for the velocity and "zeroGradient" for the pressure (OpenFOAM documentation, 2020). Given the high computational costs, the wave front was located 50 m upstream of the dam (Fig. 1) to reduce the length of the domain and the time of simulation. A simulation time of 5 s took approximately 6.5 days of computation time with 80 CPU cores and 600 GB of memory.

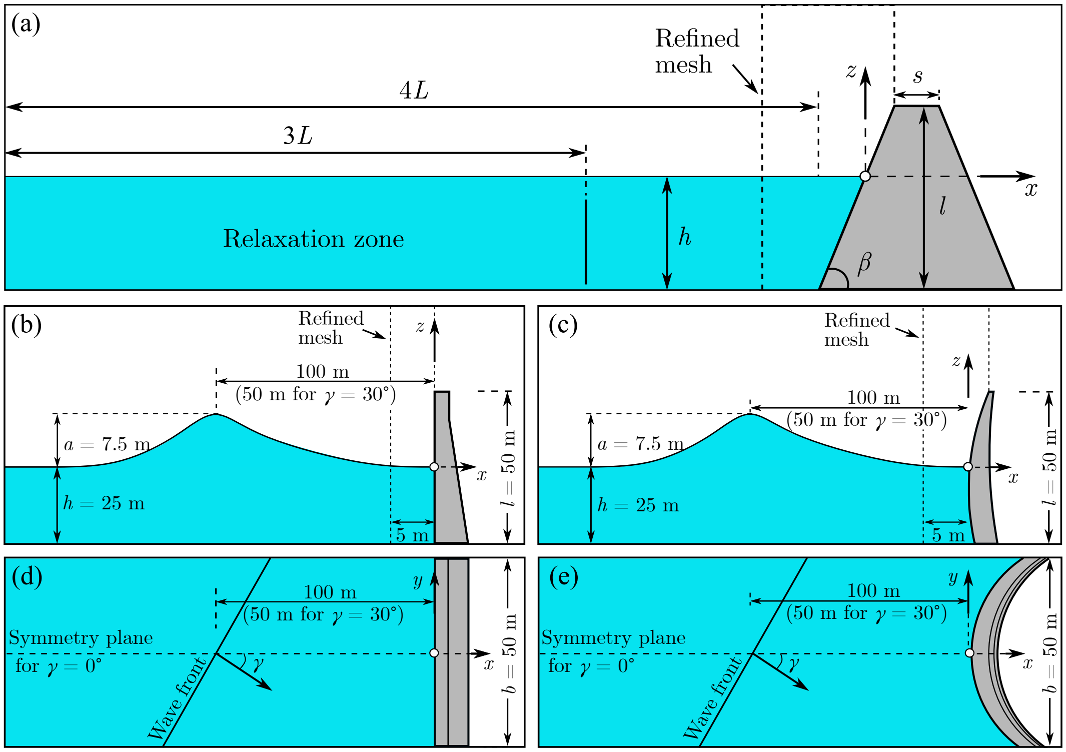


**Fig. 1.** Numerical set-ups: (a) 2D tests, (b,c) lateral and (d,e) top views of the 3D tests with (b,d) showing the gravity and (c,e) the arch dam.

# 3. Results

## *3.1. Validation of the numerical toolbox*

### *3.1.1. Comparison with experiments and an analytical solution*

The numerical toolbox was validated with the laboratory measurements of Mallayachari and Sundar (1995) and the analytical solution of Tadjbakhsh and Keller (1960) for linear waves impacting a vertical wall. The numerical simulations were conducted with the identical set-up as in Mallayachari and Sundar (1995). A mesh resolution of $\Delta x = \Delta z = 0.0015$ m was employed, resulting from the convergence analysis in Appendix B.2. The dynamic pressure $p_d$ (Dean and Dalrymple, 1991), defined as

$$p_d(z) = \begin{cases} p(z) & \text{for } 0 < z \leq \eta, \\ p(z) + \rho g z & \text{for } -h \leq z \leq 0, \end{cases} \tag{11}$$

where $p(z)$ is the measured pressure in the simulations, is compared with the experimental and analytical results for two selected tests with intermediate-water waves in Fig. 2.

The analytical solution $p_{lin}$ takes only the linear term into account whereas $p_{nonlin}$ considers up to the third order term (Tadjbakhsh and Keller, 1960). The normalised root mean square error

$$nRMSE = \frac{\sqrt{\frac{1}{\mathrm{N_d}} \sum_{\mathrm{i}}^{\mathrm{N_d}} \left(p_{d,ref,\mathrm{i}} - p_{d,num,\mathrm{i}}\right)^2}}{\left(p_{d,num,max} - p_{d,num,min}\right)} \tag{12}$$

was computed, with the experimental or analytical (subscript $ref$) and the numerical (subscript $num$) value, respectively, $\mathrm{N_d}$ is the number of considered $p_d$ values and the subscripts $max$ and $min$ stand for the maximum and minimum values. Eq. (12) was applied for $z \leq 0$ m only, due to the lack of experimental data for $z > 0$ m. In addition, the analytical solution does not result in atmospheric pressure ($p_d = 0$) as observed in the simulations at $z = \eta$ (Fig. 2). In both experiments the numerical toolbox captures the experimental data and the analytical model well. This resulted in $nRMSE = 0.14$ and 0.08 for the experimental data in Fig. 2a,b, respectively, and $nRMSE = 0.07$ to 0.14 and 0.02 to 0.21 for the analytical solution in Fig. 2a,b, respectively.

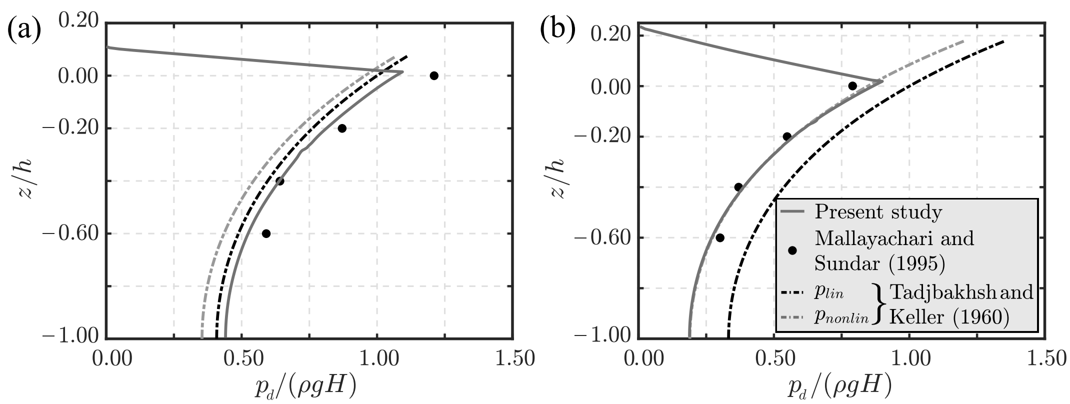


**Fig. 2.** Comparison of the numerical pressure $p_d/(\rho g H)$ versus $z/h$ with laboratory measurements (Mallayachari and Sundar, 1995) and analytical $p_{lin}$ and $p_{nonlin}$ (Tadjbakhsh and Keller, 1960) for (a) $H = 0.023$ m and $T = 0.950$ s and (b) $H = 0.048$ m and $T = 0.873$ s (after Attili et al., 2020).

### 3.1.2. Comparison with numerical solutions

The time series of the solitary wave forces $F$ at a vertical dam were compared with the numerical results of Cooker et al. (1997). The numerical simulations herein were performed with the set-up shown in Fig. 1a, for $0.1 \leq a/h \leq 0.5$. The dimensionless force $F/(\rho g h^2)$ versus the dimensionless time $(t - t_0)(g/h)^{0.5}$ is shown in Fig. 3, where $t_0$ is the instant when the maximum $R$ occurs. The present study is in good agreement with Cooker et al. (1997), showing a maximum deviation of only 5% for $a/h = 0.5$ at $t = t_0$. In further agreement, $F$ is maximum at $t = t_0$ for $a/h \leq 0.3$, while a double peak is observed in proximity of $t = t_0$ for $a/h \geq 0.4$ (Fig. 3).

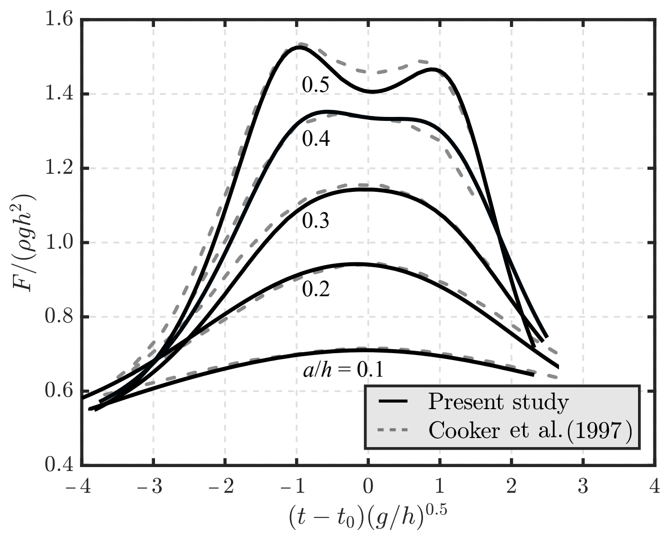


**Fig. 3.** Comparison of the time series of the dimensionless forces $F/(\rho g h^2)$ at the dam with that of Cooker et al. (1997) for $a/h = 0.1, 0.2, 0.3$, and 0.5.

### 3.1.3. Validation for overtopping waves with laboratory experiments

The numerical solver was validated with 2 laboratory experiments of Kobel et al. (2017) for the overtopping volume $\forall$ and depth $d_0$ of solitary waves impacting a vertical dam. The numerical set-up consisted of a 2D wave flume with a 0.30 m high plate representing the dam and $h = 0.25$ m. A mesh resolution of $\Delta x = \Delta z = 1.50$ mm was employed (Appendix B).

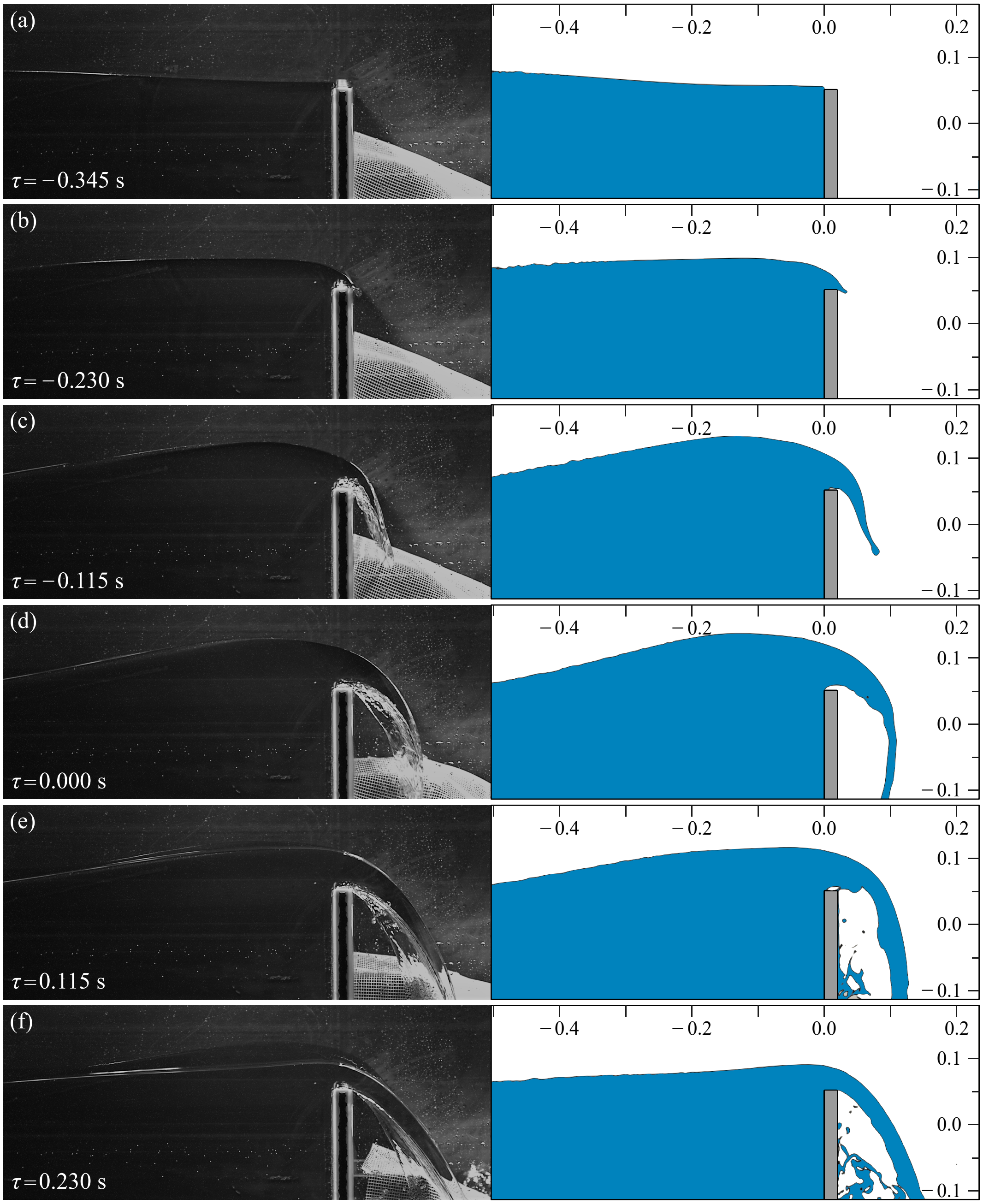


**Fig. 4.** Comparison between laboratory (Kobel et al., 2017) and numerical snapshot series of a solitary wave impact on a vertical dam with overtoppings with $a/h = 0.30$. The units of the $x$ and $z$ axes are m.

The comparison between laboratory and numerical results for experiment 1 (Table 2) is shown in Fig. 4 for a section of the wave flume of approximatively 0.85 m $\times$ 0.30 m. The free water surface is compared at several adjusted times $\tau = t - t_{d0}$, with $t_{d0}$ as the time during the maximum $d_0$. This reveals that the main features of the phenomenon are captured by the simulation. The experimental (subscript *exp*) and numerical $\cancel{V}/h^2$ and $d_0/h$ are addressed in Table 2. The numerical $\cancel{V}/h^2$ and $d_0/h$ are well predicted in both experiments with a maximum deviation of 14%.

**Table 2**
Overview of the main parameters in the comparison with experiments of Kobel et al. (2017).

| Experiment | $a/h$ | $\frac{\cancel{V}_{exp}}{h^2}$ | $\frac{\cancel{V}_{num}}{h^2}$ | $\Delta \cancel{V}$ | $\frac{d_{0,exp}}{h}$ | $\frac{d_{0,num}}{h}$ | $\Delta d_0$ |
|---|---|---|---|---|---|---|---|
| 1 | 0.30 | 0.25 | 0.27 | 8% | 0.28 | 0.27 | 4% |
| 2 | 0.50 | 0.55 | 0.60 | 9% | 0.56 | 0.64 | 14% |

### *3.2. No overtopping*

The tsunamis travelled along the numerical flume, impacted and run-up the dam before being reflected. This is shown in the snapshot series in Fig. 5 for a solitary wave with $a/h = 0.31$ and $\beta = 90°$.

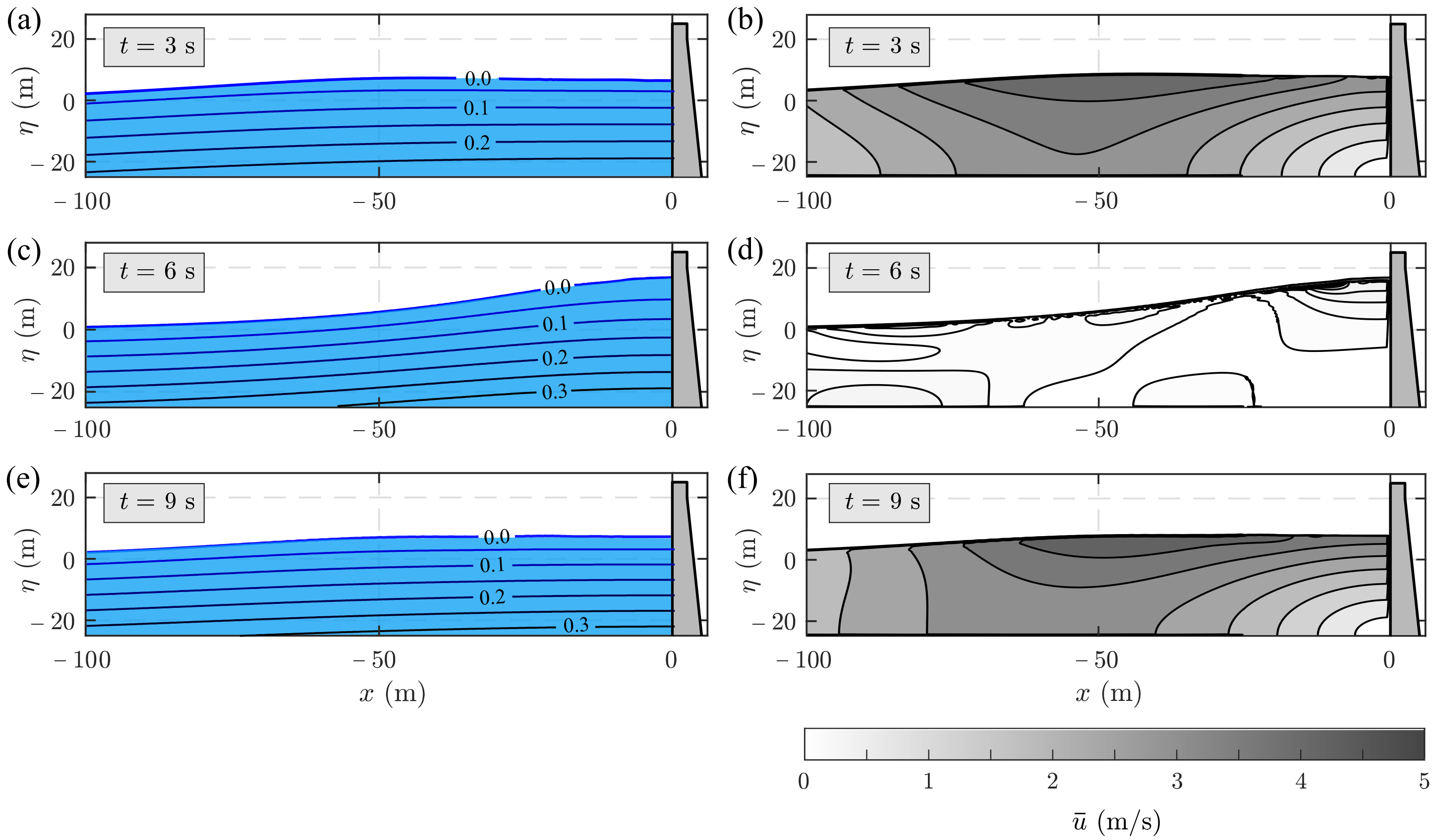


**Fig. 5.** Snapshot series of a solitary wave impact on a dam without overtopping with $a/h = 0.31$ with (a,c,e) pressure contours in MPa and (b,d,f) mean velocity $\bar{u} = \sqrt{\bar{u}_x^2 + \bar{u}_z^2}$ contours.

### *3.2.1. Run-up*

The simulations to investigate the run-up heights $R$ at the dam were conducted with smooth slopes. Although they do not represent all types of dam surfaces, Teng et al. (2000) found that the effects of the roughness on $R$ can be neglected for relatively steep slopes $\beta \geq 20°$.

The maximum $R/h$ observed in each test is shown in Fig. 6a versus $a/h$. In agreement with Cooker et al. (1997), the instant $t_0$ (Section 3.1.2) does not necessarily coincide with $t$ when the maximum $F$ is observed (Fig. 3). $R/h$ increases with $a/h$ following approximately a linear trend (Fig. 6a). Some of the cnoidal wave tests with $\beta = 60$ or $75°$ show larger values compared to the other tests for the same $a/h$. This is due to the smaller $\beta$ resulting in larger $R$, as also observed for the solitary tests (Fig. 6a) and the splash generated during the wave impacts in these simulations.

Using the linear trend between $R$ and $a/h$ shown in Fig. 6a, $R/h$ was approximated as

$$\frac{R}{h} = \frac{9}{4}\left(\frac{90}{\beta}\right)^{1/3}\frac{a}{h}, \tag{13}$$

where the pre-term and exponent were optimised through a regression analysis based on the least-square approach algorithm trust-region (Fig. 6b). The coefficient of determination

$$R^2 = 1 - \frac{\sum_{\mathrm{i}}\left(y_{num,\mathrm{i}} - y_{pred,\mathrm{i}}\right)^2}{\sum_{\mathrm{i}}\left(y_{num,\mathrm{i}} - \bar{y}\right)^2}, \tag{14}$$

was computed with $y_{num,\mathrm{i}}$ as the numerical values, $\bar{y}$ as the mean of the numerical values and $y_{pred,\mathrm{i}}$ as the predicted values (subscript *pred*).

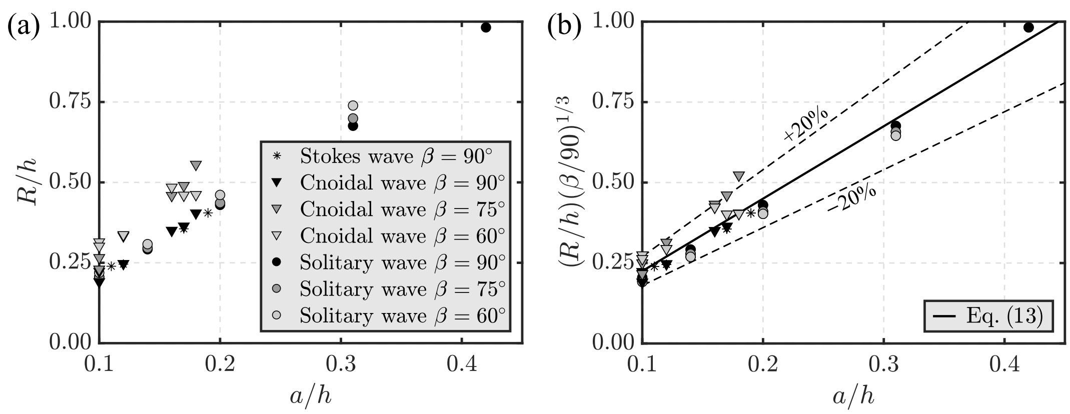


**Fig. 6.** (a) Relative run-up height $R/h$ and (b) $(R/h)(\beta/90)^{1/3}$ with Eq. (13) ($R^2 = 0.94$) versus the relative wave amplitude $a/h$.

### *3.2.2. Force and bending moment*

The horizontal force $F_H$ and bending moment $M_H$ are compared with predictions based on Evers et al. (2019). For the tests with $\beta = 60$ and $75°$, $F_H = F\sin\beta$ and $M_H = F_H z_H$ were computed, with $z_H$ as the elevation of the resultant of $F_H$ from $-h$. $F_H$ and $M_H$ are normalised with the hydrostatic force $F_h = (1/2)\rho g(2a+h)^2$ and moment $M_h = (1/6)\rho g(2a+h)^3$, respectively. $F_H/F_h$ and $M_H/M_h$ are shown with double logarithmic axes in Fig. 7 together with the predictions from Evers et al. (2019) (Eqs. 1 and 2) and the experimental data of Ramsden (1996).

Eqs. (1) and (2) predict the numerical $F_H$ and $M_H$ well, operating on the safe side, and most of the data are within the ±10% bounds (Fig. 7). The 4 tests conducted with Stokes waves represent less extreme cases with approximately 10% smaller wave loadings than predicted with Evers et al. (2019) (Fig. 7). Marginally higher values for $F_H$ and $M_H$ of the cnoidal waves for larger $T$ are observed. However, this dependence on $T$ may be neglected for the investigated range $7.2 \leq T(g/h)^{0.5} \leq 18.8$ such that Eqs. (1) and (2) deliver also good approximations for cnoidal waves. The solitary wave loadings on the dam are in good agreement with Eqs. (1) and (2).

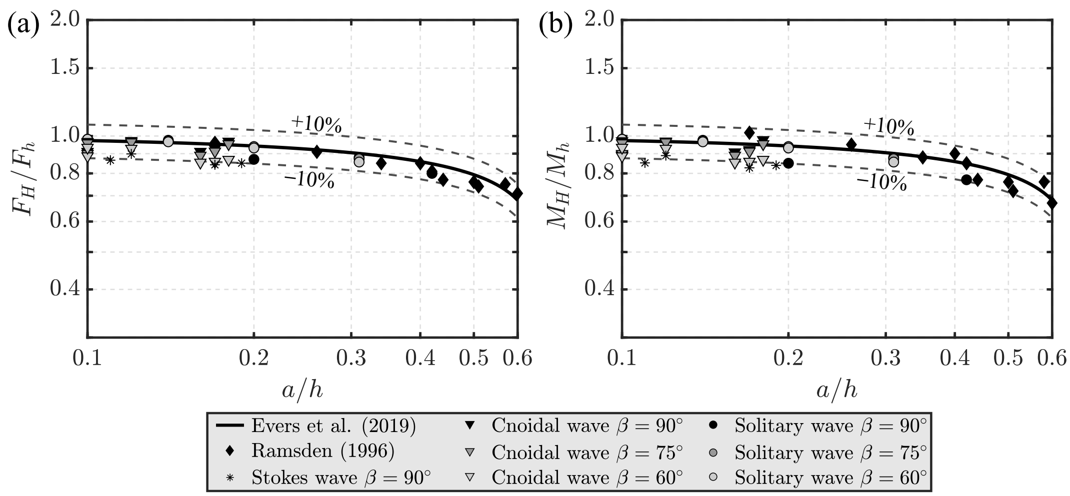


**Fig. 7.** Comparison of the horizontal dimensionless (a) force $F_H/F_h$ and (b) moment $M_H/M_h$ at the dam versus $a/h$ with predictions from Evers et al. (2019) and data of Ramsden (1996).

### *3.2.3. Dynamic pressure*

The total pressure $p$ at the wall is composed of the dynamic $p_d$ and hydrostatic $-\rho g z$ components. The component $p_d$ represents the excess pressure due to the waves, corresponding to $p$ above $(z > 0)$ and to $p + \rho g z$ below the still water surface $(z \leq 0)$ (Eq. 11).

According to Dean and Dalrymple (1991), the pressure field of linear waves propagating offshore in a water body can be determined from the unsteady Bernoulli equation resulting in $p_d = K_p(z)p(z = 0)$, for $z \leq 0$. $K_p$ is the pressure response factor

$$K_p(z) = \frac{\cosh[k(h + z)]}{\cosh(kh)}, \tag{15}$$

where $k = 2\pi/L$ is the wave number. $K_p$ reaches the maximum value of 1 at $z = 0$ and decreases for $z < 0$ proportionally to $\cosh(h + z)$.

The unsteady Bernoulli equation can also be used to describe the pressure field of waves impacting walls (Tadjbakhsh and Keller, 1960). In order to define $p_d$ of nonlinear waves impacting dams, in analogy to Dean and Dalrymple (1991), the pressure response factor at the wall (subscript $w$) $K_{pw}$ is introduced herein such that

$$p_d(z) = \begin{cases} p(z) & \text{for } z > 0, \\ K_{pw}p(z = 0) & \text{for } -h \leq z \leq 0, \end{cases} \tag{16}$$

where $p(z)$ can be predicted with Eq. (3) (Evers et al., 2019).

Despite of the different conditions compared to linear waves propagating offshore in a water body, $K_{pw}$ in the numerical tests showed similar trends as $K_p$ (Eq. 15) and are approximated in function of $a/h$, $z/h$ and a coefficient $A$ as

$$K_{pw}(a/h, z/h) = \frac{\cosh[A(a/h)(1 + z/h)]}{\cosh[A(a/h)]}. \tag{17}$$

$A$ was optimised for each test with a least squares regression analysis resulting in $1.28 \leq A \leq 15.06$. Eq. (17) captures the numerical results well with coefficients of determination of $R^2 = 0.95$ to 1.00, as shown in Fig. 8 for 4 representative tests.

To eventually express $K_{pw}$ as a function of $a/h$ and $z/h$ only, the coefficients $A$ were defined separately for Stokes and cnoidal (Eq. 18) and solitary waves (Eq. 19) with

$$A = (a/h)^{-1} \text{ and} \tag{18}$$

$$A = (a/h)^{-2/3}. \tag{19}$$

Eq. (19) captures the data within deviations of ±20% for the solitary waves (Fig. 9b), while larger deviations are observed for Eq. (18) for Stokes and cnoidal waves (Fig. 9a). However, most of the data lie within the ±30% bounds. Combining Eq. (17) with Eqs. (18) and (19) results in

$$K_{pw}(z/h) = \frac{\cosh(1 + z/h)}{\cosh(1)}, \text{for Stokes and cnoidal waves and} \tag{20}$$

$$K_{pw}(a/h, z/h) = \frac{\cosh[(a/h)^{1/3}(1 + z/h)]}{\cosh[(a/h)^{1/3}]}, \text{for solitary waves.} \tag{21}$$

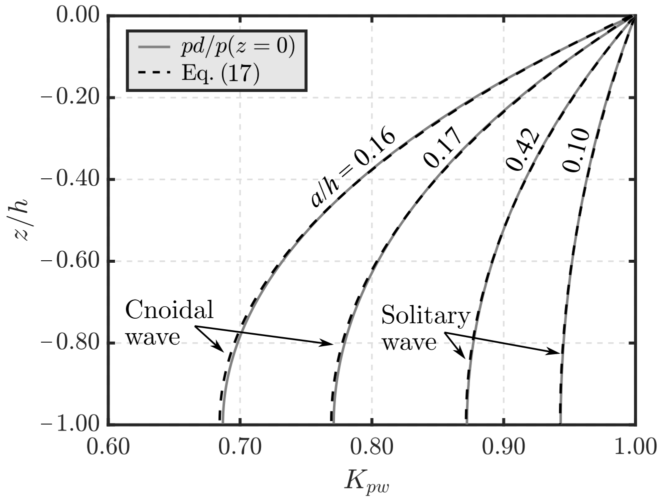


**Fig. 8.** Distribution of the pressure response factor at the wall $K_{pw}$ with $z/h$ for $\beta = 90°$ and Eq. (17) for $a/h = 0.10$ ($R^2 = 1.00$), 0.16 ($R^2 = 1.00$), 0.17 ($R^2 = 1.00$), and 0.42 ($R^2 = 1.00$) and $A = 3.47, 5.79, 4.45$, and 1.28, respectively.

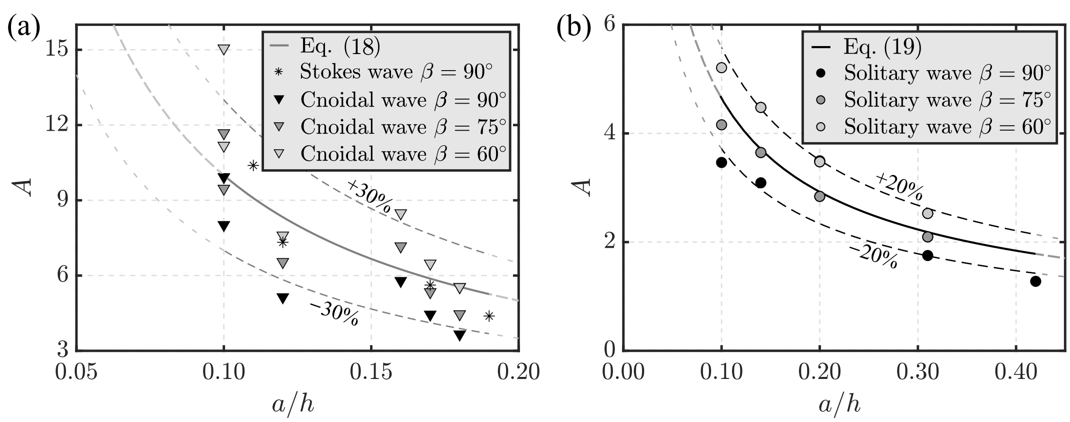


**Fig. 9.** Coefficient $A$ versus the relative wave amplitude $a/h$ and (a) Eq. (18) for Stokes and cnoidal waves ($R^2 = 0.59$) and (b) Eq. (19) for solitary waves ($R^2 = 0.72$).

Eq. (21) shows that $K_{pw}$ decays slower with $z/h$ for smaller $a/h$ than in Eq. (20). $K_{pw}$ for Stokes and cnoidal waves is a function of $z/h$ only and would coincidence with Eq. (21) for $a \to h$. Therefore, Eq. (21) operates on the safe side for $a/h < 1$ and can be used for Stokes and cnoidal waves also, i.e. the wave type does not need to be determined.

To summarise, semi-empirical equations for the pressure response factor at the wall $K_{pw}$ were presented in this Section 3.2.3. These Eqs. (20) and (21), combined with the prediction of the total pressure $p$ from Evers et al. (2019) (Eq. 3), directly provide the dynamic component of the pressure $p_d$ (Eq. 16). To confirm these equations, the numerical $p(z)$ and $p_d(z)$ are compared with predictions of Evers et al. (2019) ($nRMSE = 0.017$ to $0.043$) and Eq. (16) ($nRMSE = 0.04$ to $0.14$) in Fig. 10 for 4 representative tests. The good agreement confirms the suitability of the new semi-empirical equations for engineering applications.

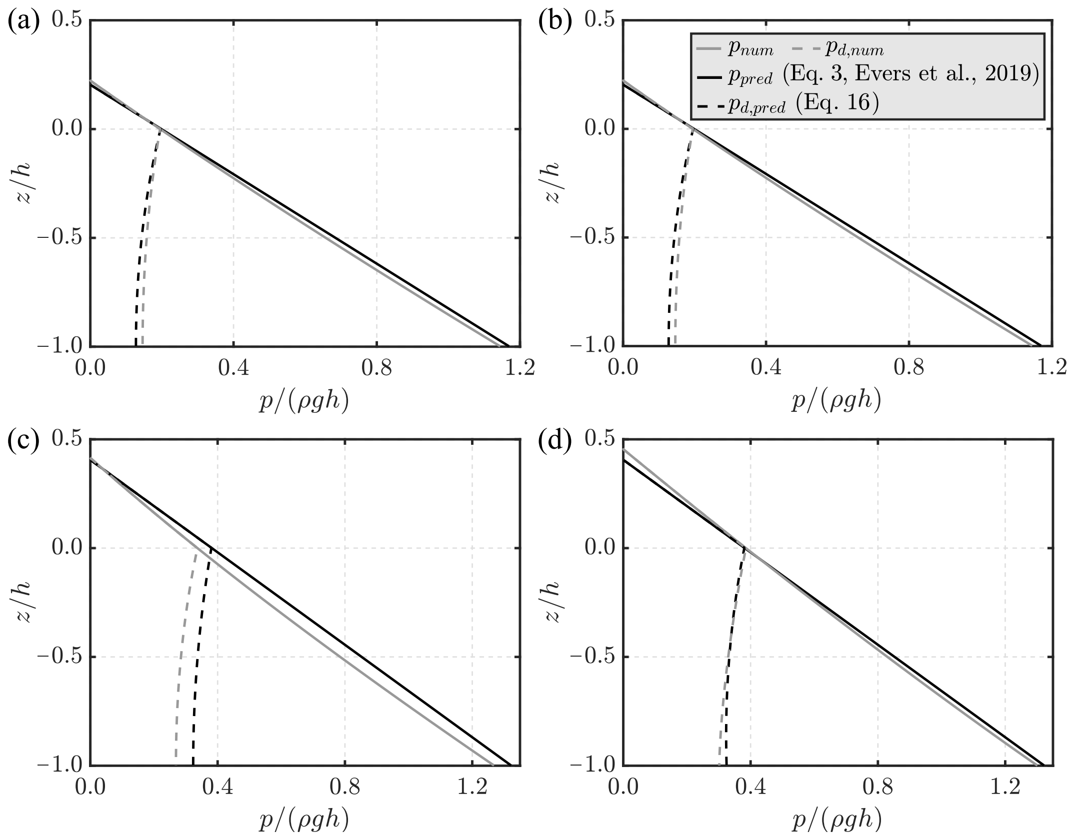


**Fig. 10.** Comparison of the total $p/(\rho g h)$ and dynamic pressure $p_d/(\rho g h)$ with predictions from Evers et al. (2019) (Eq. 3) and Eq. (16) for cnoidal waves with $a/h = 0.10$ and (a) $\beta = 90$ and (b) $60°$ and solitary waves with $a/h = 0.20$ and (c) $\beta = 90$ and (d) $60°$.

### 3.3. Overtopping waves

#### 3.3.1. Force and bending moment

In 37 of the 72 tests (Table 1) $R$ exceeded the freeboard $f$ and the waves overtopped the dam, as shown in Fig. 11 for a solitary wave with $a/h = 0.28$, $f = 14$ m, and $\beta = 90°$. In these cases, only a part of the wave loading is transferred on the dam (Appendix A). The ratios $F_{H,red}/F_h$ and $M_{H,red}/M_h$ versus $a/h$ are shown in Fig. 12a,c. Moreover, Fig. 12b,d shows $F_{H,red}/F_h$ and $M_{H,red}/M_h$ versus $f/h$. $F_{H,red}/F_h$ and $M_{H,red}/M_h$ decrease with increasing $a/h$ for a constant $f/h$, except for the solitary wave test with $a/h = 0.6$ and $\beta = 90°$, whereas larger $f/h$ result in larger wave loadings for a constant $a/h$ (Fig. 12b,d).

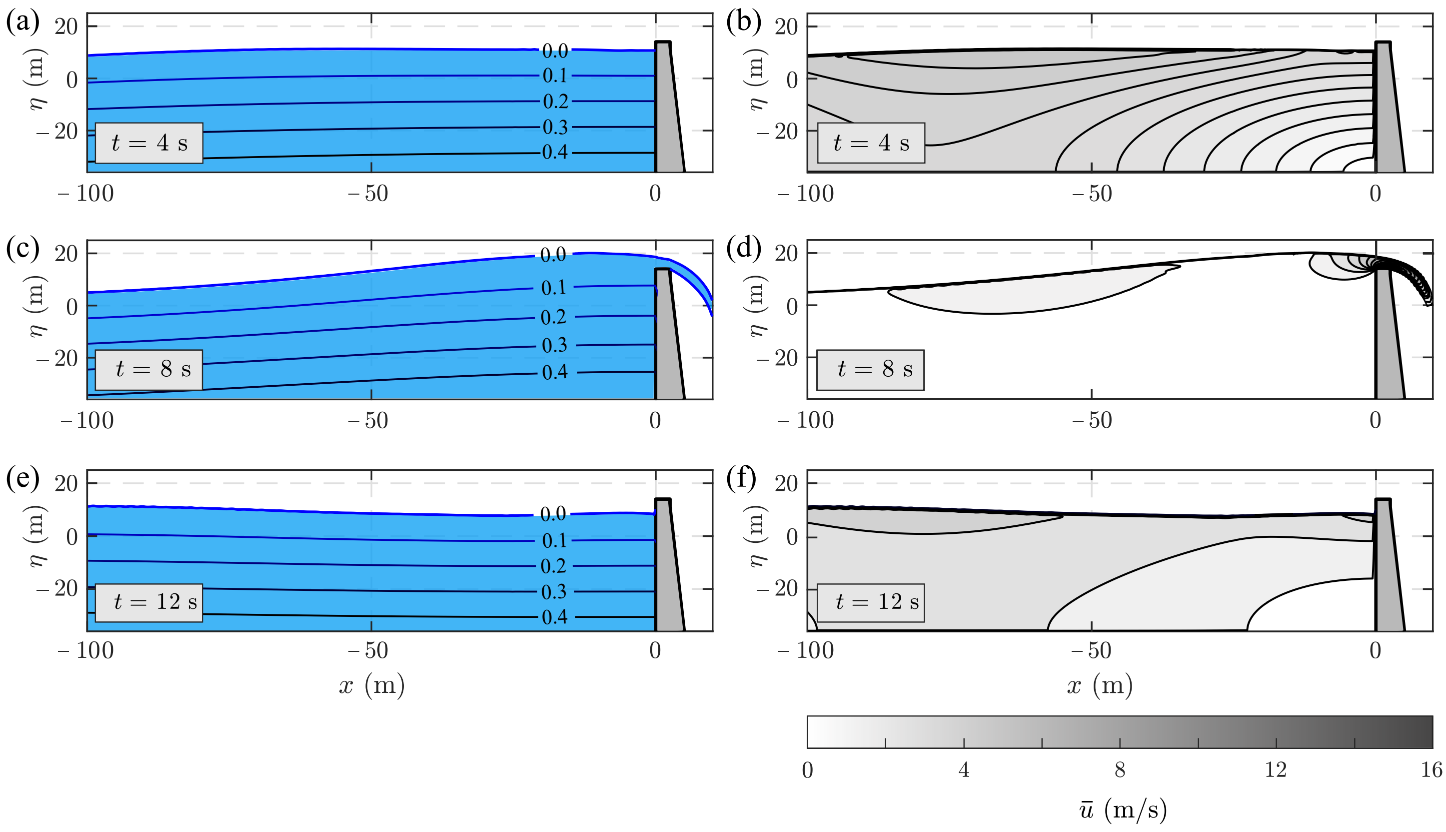


**Fig. 11.** Snapshot series of a solitary wave impact on a dam with overtopping with $a/h = 0.28$ with (a,c,e) pressure contours in MPa and (b,d,f) mean velocity $\bar{u}$ contours.

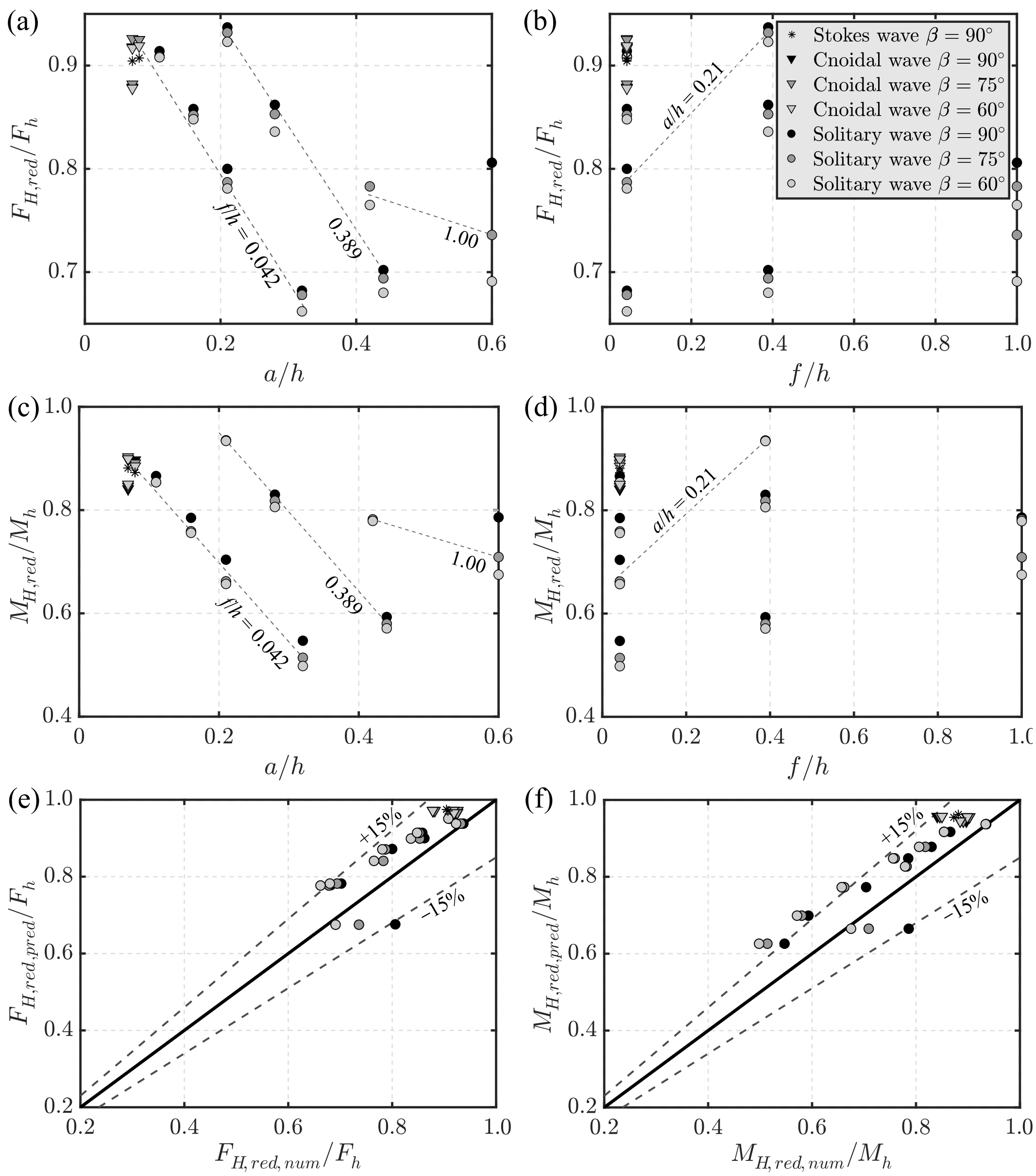


**Fig. 12.** Overtopping waves: relative reduced horizontal force $F_{H,red}/F_h$ versus (a) $a/h$ and (b) $f/h$, moment $M_{H,red}/M_h$ versus (c) $a/h$ and (d) $f/h$, and comparison of the predicted (Evers et al., 2019) and numerical (e) $F_{H,red}/F_h$ and (f) $M_{H,red}/M_h$ at the dam.

Fig. 12e,f shows $F_{H,red}$ and $M_{H,red}$ versus the predicted values for $F_{H,red}$ and $M_{H,red}$ based on Evers et al. (2019). Their method disregarding the top part of the pressure distribution on $F_H$ and $M_H$ (Appendix A) agrees with the numerical results. This method results in predictions of $F_{H,red}$ and $M_{H,red}$ on the safe side for most of the experiments with deviations of up to approximately 15 and 20%, respectively (Fig. 12e,f).

Only the 3 solitary waves with $a/h = 0.6$ are underestimated, namely by up to 19%, compared to the numerical results (Fig. 12e,f). In these extreme cases, due to the relatively large wave steepness $a/L \approx 0.065$ (with $L$ from Eq. 25), surging breaking was initiated in proximity of the dam. Surging breakers usually occur in proximity of steep slopes and are characterised by little foam (Galvin, 1968). Surging breaking may be the reason for the observed deviations.

*3.3.2. Overtopping*

The overtopping volume per unit dam width $\mathcal{V}$ and the maximum overtopping depth over the dam crest $d_0$ were also investigated. The numerical toolbox was first validated with the laboratory experiments of Kobel et al. (2017) (Section 3.1.3). $\mathcal{V}$ was evaluated at the upstream corner of the dam crest as

$$\mathcal{V} = \sum_t \frac{q(t) + q(t+1)}{2} \Delta t, \tag{22}$$

with the discharge per unit dam width $q(t)$ defined as $\sum_z \bar{u}_x(z)\Delta z$, for $f \leq z \leq (f + d_0)$.

$\mathcal{V}/h^2$ and $d_0/h$ are shown in function of $a/h$ in Fig. 13. Both $\mathcal{V}/h^2$ and $d_0/h$ increase with increasing $a/h$ for a constant $f/h$, except for the solitary wave with $a/h = 0.6$ and $\beta = 90°$. In this test the splash generated during wave impact may explain the relatively larger values of $d_0/h$ compared to the remaining tests (Fig. 13b).

In addition to $a/h$, $\beta$ and $f/h$ have also a significant effect on the investigated parameters. Smaller $\beta$ result in smaller $\mathcal{V}/h^2$ and larger $d_0/h$ (Fig. 13a), while both $\mathcal{V}/h^2$ and $d_0/h$ decrease with increasing $f/h$. An exception is once more the solitary wave with $a/h = 0.6$ and $\beta = 90°$.

For the Stokes and cnoidal wave tests, the effects of $T$ on $\mathcal{V}$ and $d_0$ are also important. They become even more relevant in combination with the effects of $a/h$ and $\beta$. In the cnoidal wave tests with $\beta = 90°$, an increase of $T$ by 33% results in a 25% larger $\mathcal{V}$. The same increase of $T$ resulted in 77 and 96% greater $\mathcal{V}$ for $\beta = 60$ and 75°, respectively.

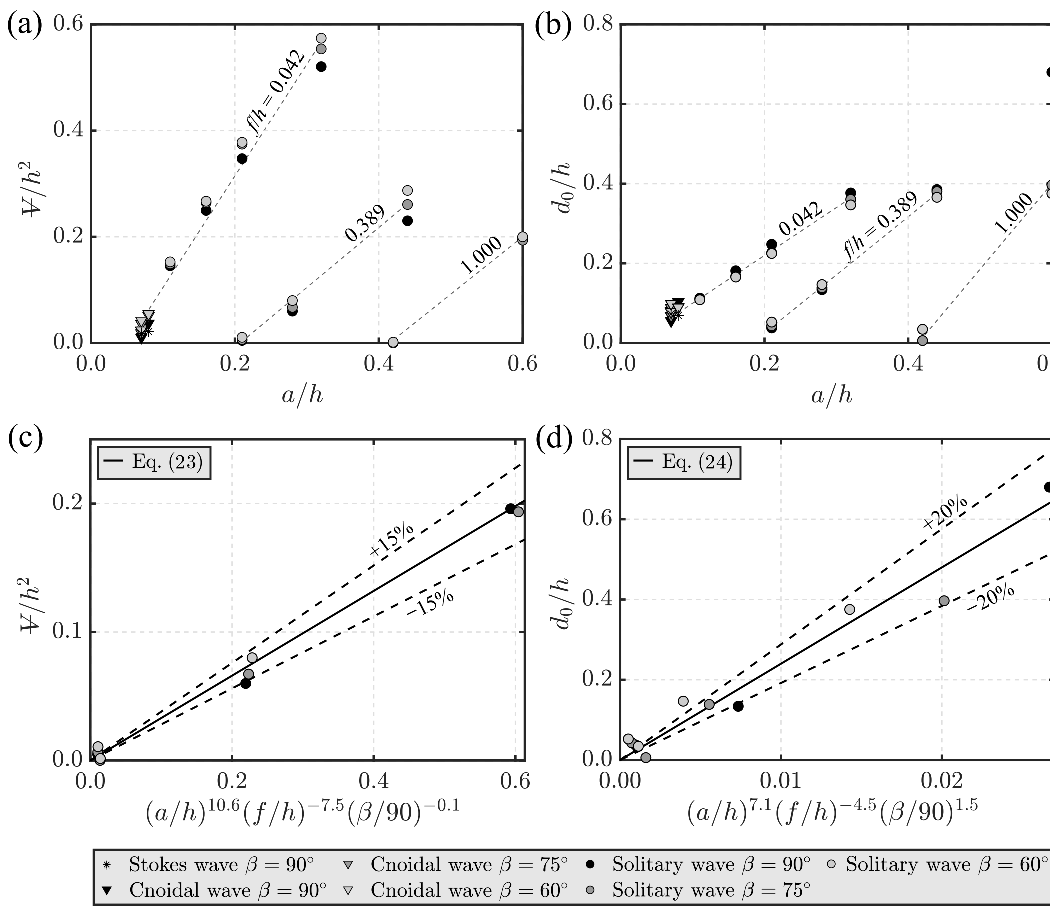


**Fig. 13.** Relative overtopping (a) volume $\forall/h^2$ and (b) maximum depth $d_0/h$ versus $a/h$ and correlations of (c) $\forall/h^2$ with Eq. (23) ($R^2 = 0.99$) and (d) $d_0/h$ with Eq. (24) ($R^2 = 0.96$).

$\forall/h^2$ and $d_0/h$ can be predicted with the empirical equations of Kobel et al. (2017) (Eqs. 26 and 27). They are compared with the present data in Section 4.3. However, for $a \leq f$, Eq. (26) cannot be applied and Eq. (27) is in poor agreement with the present study. Based on the numerical data, $\forall/h^2$ and $d_0/h$ were approximated for $a \leq f$ in function of $a$, $f$, $h$, and $\beta$ as

$$\frac{\forall}{h^2} = 44\left(\frac{a}{h}\right)^{10.6}\left(\frac{f}{h}\right)^{-7.5}\left(\frac{\beta}{90}\right)^{-0.1} \quad \text{and} \tag{23}$$

$$\frac{d_0}{h} = 24\left(\frac{a}{h}\right)^{7.1}\left(\frac{f}{h}\right)^{-4.5}\left(\frac{\beta}{90}\right)^{1.5}. \tag{24}$$

These correlations were optimised with a least-squares regression analysis and are shown in Fig. 13c,d together with the numerical data. The aforementioned effects of each parameter are consistent with the pre-sign of the exponents in Eqs. (23) and (24) and for both equations the most dominant parameter resulted in $a/h$, followed by $f/h$.

## 4. Discussion of results

### *4.1. Validation of the available prediction method and limitations*

The prediction method for tsunami forces on dams of Evers et al. (2019) was validated for a wide range of wave conditions and dam inclinations with 72 numerical tests (Figs. 7 and 12e,f). The numerical experiments replicate hypothetical, yet realistic, cases at real-world scale without scale effects (Heller, 2011; Bredmose et al., 2015). To apply Eqs. (1) and (2) and the equations for waves with overtoppings (Appendix A) in nature, the dimensionless wave parameters need to be within the investigated ranges, i.e., $0.07 \leq a/h \leq 0.60$, $0.13 \leq H/h \leq 0.26$, and $7.2 \leq T(g/h)^{0.5} \leq 18.8$, for 5th order Stokes, cnoidal and/or solitary waves, and dam inclinations of $60° \leq \beta \leq 90°$.

Table 3 includes some historical subaerial landslide-tsunamis. The dimensionless maximum $a/h$ and $T(g/h)^{0.5}$ for these events are all within the limits of the present study, apart from $T(g/h)^{0.5}$ of the Lake Askja event. Further, the investigated values for $\beta$ in the present study are typical for concrete dams.

**Table 3**
Main parameters of some subaerial landslide-tsunami events.

| Event | $h$ [m] | $a/h$ [-] | $T(g/h)^{0.5}$ [-] | References |
|---|---|---|---|---|
| Pontesei Lake, 1959 | 47 | 0.40 | Not available | Panizzo et al. (2005a) |
| Cabrera Lake, 1965 | 50 to 200 | 0.125 to 0.500 | Not available | Watt et al. (2009) |
| Chehalis Lake, 2007 | 120 | 0.47 | 9.35 | Wang et al. (2015); Evers (2017) |
| Lake Askja, 2014 | 138 | 0.25 | 6.30 | Gylfadóttir et al. (2017); Ruffini et al. (2019) |

### *4.2. Run-up height*

Predictions with Eq. (13) are compared with laboratory measurements of Street and Camfield (1967), Maxworthy (1976), and Müller (1995) (Table 4) in Fig. 14a. Only data within the limitations of $\beta$ of the present study were selected. The predicted $R/h$ capture the experimental $R/h$ and most of the tests lie within $\pm 20\%$ of the prediction.

Fig. 14b shows the predicted $R/h$ with the equations included in Table 4 versus the numerical $R/h$ from the present study. Hall and Watts (1953) and Evers and Boes (2019) expressed $R/h$ as a function of $a/h$ and $\beta$ only, while Müller (1995) includes $H/h$, $H/L$, and $\beta$ (Table 4). This requires the wave length for solitary waves, which can be approximated as (Lo et al., 2013)

$$L = 2\pi h/(0.75a/h)^{0.5}. \tag{25}$$

**Table 4**
Predictions and limitations of the run-up height $R$ in the present and other studies.

| Reference | $R/h$ | Limitations |
|---|---|---|
| Hall and Watts (1953) | $3.05\tan(\beta)^{-0.13}\left(\frac{a}{h}\right)^{1.15\tan(\beta)^{0.02}}$ | $0.050 \leq a/h \leq 0.564$, $10° \leq \beta \leq 45°$ |
| Street and Camfield (1967) | No empirical equation available | $0.100 \leq a/h \leq 0.645$, $\beta = 90°$ |
| Maxworthy (1976) | No empirical equation available | $0.118 \leq a/h \leq 0.665$, $\beta = 90°$ |
| Müller (1995) | $1.25\left(\frac{H}{h}\right)^{5/4}\left(\frac{H}{L}\right)^{-3/20}\left(\frac{90°}{\beta}\right)^{1/5}$ | $0.011 \leq a/h \leq 0.521$, $18.4° \leq \beta \leq 90°$ |
| Evers and Boes (2019) | $2\frac{a}{h}\exp\left(0.4\frac{a}{h}\right)\left(\frac{90°}{\beta}\right)^{0.20}$ | $0.007 \leq a/h \leq 0.690$, $10° \leq \beta \leq 90°$ |
| Eq. (13) | $\frac{9}{4}\left(\frac{90}{\beta}\right)^{1/3}\frac{a}{h}$ | $0.100 \leq a/h \leq 0.420$, $60° \leq \beta \leq 90°$ |

Hall and Watts (1953) are applied for $\beta = 60$ and $75°$ only, as their equation involves the tangent of the inclination $\beta$ preventing estimates for $\beta = 90°$. The equation of Hall and Watts (1953) underestimates the numerical $R/h$ by up to 64%, apart from a few tests. These deviations are partially due to the violation of the limitations of $\beta$ (Table 4). The equation of Müller (1995) successfully predicts most of the cnoidal wave tests, while the solitary waves are underestimated by up to 42%. Similar agreements are achieved by Evers and Boes (2019) and Eq. (13) based on the numerical $R/h$. Most of the tests show relatively small deviations and only a few cases are underestimated, namely by up to 39% by the equation of Evers and Boes (2019) and by up to 32% by Eq. (13) (Fig. 14b).

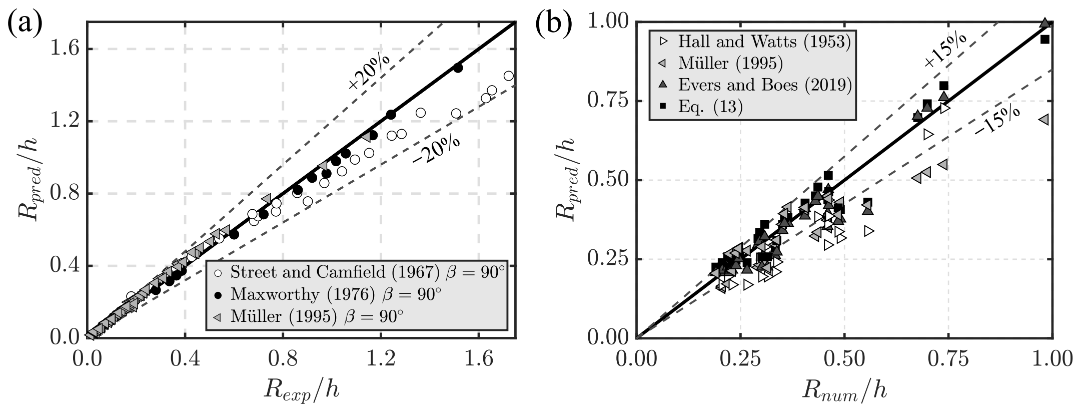


**Fig. 14.** Predicted relative run-up heights $R_{pred}/h$ (a) based on Eq. (13) versus the experimental $R_{exp}/h$ of Street and Camfield (1967), Maxworthy (1976), and Müller (1995) with $\beta = 90°$ and (b) based on Hall and Watts (1953), Müller (1995), Evers and Boes (2019), and Eq. (13) (Table 4) versus the numerical $R_{num}/h$ of the present study.

### *4.3. Overtopping*

The overtopping volume $\cancel{V}$ and the maximum overtopping depth over the dam crest $d_0$ (Section 3.3.2) are compared with the empirical predictions of Kobel et al. (2017), which are

$$\cancel{V} = 1.35\left(\frac{a}{H}\right)^{1.5}\left[\frac{a}{h}\left(\frac{h}{l}\right)^{(2h/a)(\beta/90)^{0.25}}\left(\frac{a-f}{s}\right)^{0.12}\right]^{0.7} h^2 \text{ and} \tag{26}$$

$$d_0 = 1.32\left[\frac{a}{h}\left(\frac{h}{l}\right)^{4\left[(\beta/90)^{-0.21}-a/h\right]}\left(\frac{\beta}{90}\right)^{0.16}\right] l. \tag{27}$$

The comparison is shown in Fig. 15. For $a \leq f$, overtoppings occur due to the increase in $\eta$ once the wave is reflected at the dam and $\cancel{V}/h^2$ cannot be predicted with Eq. (26). Instead, Eq. (23) can be used. Eq. (26) successfully captures the numerical results, with most of the data showing a deviation on the safe side of less than 15%. Stokes and cnoidal waves show relatively large deviations with overestimations of up to 75%; these are attributed to the fact that Eq. (26) is based on solitary wave laboratory tests.

Fig. 15b shows the predicted $d_0/h$ with Kobel et al. (2017) and Eq. (24), applicable for $a \leq f$ only, versus the numerical $d_0/h$. Eq. (27) agrees with the numerical results for the tests with $a > f$, showing the largest deviations of up to 36% for the Stokes and cnoidal wave tests, once more because Eq. (27) is based on a different wave type. Most of the tests with $a \leq f$ (encircled data in Fig. 15b) are overpredicted by Eq. (27) with relatively large deviations. Eq. (24) results in smaller deviations, however, the prediction of the overtopping waves with $a \leq f$ remains even then challenging. Table 5 shows a summary of the most suitable equations for the prediction of wave run-ups and overtoppings.

Note that the new methods introduced herein also provide good estimates of non-breaking tsunami forces, pressures, and overtoppings for a range of steep to vertical coastal engineering structures. Therefore, such estimates support tsunami hazard assessment in coastal environments in general.

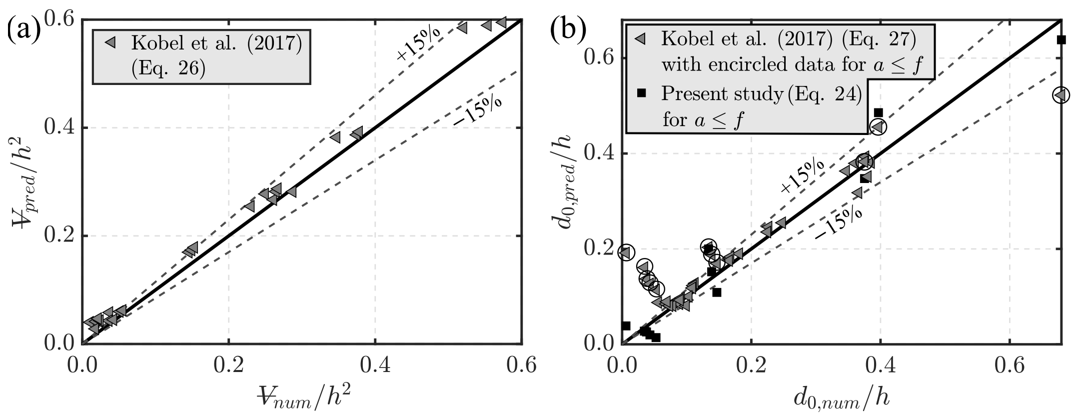


**Fig. 15.** Comparison of the predicted and numerical relative overtopping (a) volume $\cancel{V}/h^2$ and (b) maximum depth $d_0/h$ with encircled data predicted by Kobel et al. (2017) for $a \leq f$.

**Table 5**
Summary of the most suitable equations to predict landslide-tsunami run-ups and overtoppings.

| | | No overtopping | Overtopping $a \leq f$ | $a > f$ |
|---|---|---|---|---|
| Run-up height | $R$ | Eq. (13) | - | - |
| Overtopping volume | $\cancel{V}$ | - | Eq. (23) | Eq. (26) (corresponding to Eq. 2 in Kobel et al., 2017) |
| Overtopping depth | $d_0$ | - | Eq. (24) | Eq. (27) (corresponding to Eq. 4 in Kobel et al., 2017) |

### *4.4. 3D simulations to investigate 3D effects*

#### *4.4.1. Symmetrical wave impact angle*

For the gravity dam with normal wave impact ($\gamma = 0°$, Fig. 1b,d) the different boundary conditions used at $y = 0$ and 25 m result in small deviations of the main parameters, e.g. $p$ and $\alpha$, across the dam width (Section 2.2.1). $R/h$ is constant across $y/h$ and $R_{max}/h = 0.68$ agrees with the predicted value of 0.68 from Eq. (13) (Fig. 16).

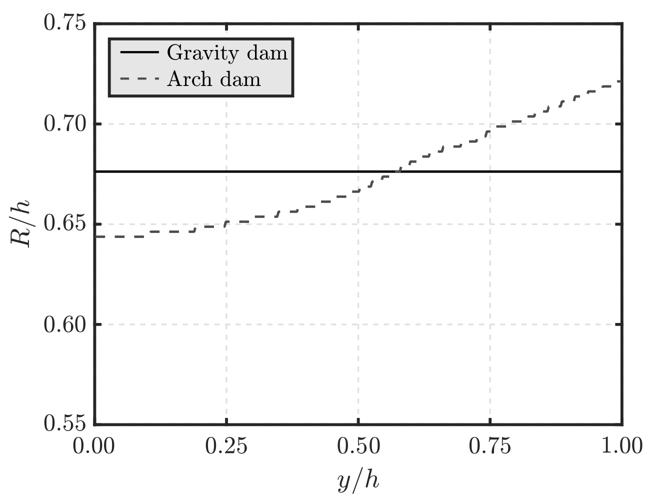


**Fig. 16.** Maximum relative run-up height $R_{max}/h$ versus $y/h$ for the gravity dam and $R/h$ versus $y/h$ for the arch dam at $t = 6.8$ s, with $a/h = 0.3$ and $\gamma = 0°$.

Fig. 16 shows $\eta/h$ across the arch dam (Fig. 1c,e) with $\gamma = 0°$ during $R_{max}/h$ at $y = 25$ m. The dam curvature induces an increase in $R/h$ of approximately 10% close to the lateral flanks of the reservoir. At $y = 0$ m, $R_{max}/h = 0.66$ at $t = 6.2$ s, which is still well captured by Eq. (13) with $\beta = 90°$. At $y = 25$ m, $R_{max}/h = 0.72$ is delayed and approximately 9% larger than at $y = 0$ m (Fig. 16).

For the arch dam, the force vector per unit dam width $\mathbf{F}$ was calculated as

$$\mathbf{F}(y,t) = \sum_{\mathrm{i}}^{\mathrm{N}} p(y, z_{\mathrm{i}}, t)\mathbf{n}_{\mathrm{i}}\Delta z, \tag{28}$$

with $p(y, z_{\mathrm{i}}, t)$ as the numerical pressure at the cell $(y, z_{\mathrm{i}})$, N as the number of $p(z)$ values, and $\mathbf{n}_{\mathrm{i}}$ as the normal vector to the dam surface. Similarly, the force vector acting over the entire dam is

$$\mathbf{F}_{3D}(t) = \sum_{\mathrm{i}}^{\mathrm{N}} \sum_{\mathrm{j}}^{\mathrm{P}} p(y_{\mathrm{i}}, z_{\mathrm{j}}, t)\mathbf{n}_{\mathrm{i,j}} S_{\mathrm{i,j}}, \tag{29}$$

with $p(y_{\mathrm{i}}, z_{\mathrm{j}}, t)$ as the numerical pressure at the cell $(y_{\mathrm{i}}, z_{\mathrm{j}})$, N and P as the number of $p$ values along $y$ and $z$, and $S_{\mathrm{i,j}}$ as the cell area. Hence, the horizontal components $F_H$ and $F_{H,3D}$ were calculated as the resultant of the $x$ and $y$ components.

Fig. 17a,b shows $F_H/F_h$ versus $y/h$ for the gravity and arch dam. The gravity dam shows constant values of $F_H/F_h$ across the width with the maximum $F_H/F_h$ overestimated by only 1.3% by the prediction based on Evers et al. (2019) (Eq. 1). A larger $F_H/F_h$ in proximity of the flanks acts on the arch dam (Fig. 17b). However, the effect of the curvature on $F_H/F_h$ may be neglected as the deviations between $y = 0$ and 25 m are only up to 4.7% and the maximum $F_H/F_h$ is only 1.3% greater compared to the prediction based on Evers et al. (2019) (Eq. 1). The maximum force acting over the whole dam $F_{H,3D}$ was normalised with $bF_h/2$, with the dam width $b = 50$ m. This resulted in 0.89 and 1.01, for the gravity and arch dam, respectively, and $p/(\rho g h)$ during the maximum $F_{3D}$ is shown in Fig. 17c,d.

### *4.4.2. Asymmetrical wave impact*

Fig. 18 shows a snapshot series in the $xy$ plane for the gravity dam and asymmetrical wave impact. In these tests the wave travelled along the wave tank with direction $\gamma = 30°$ (Fig. 1). The wave was reflected by the tank boundary at $y = -25$ m ($y/h = -1$) with a concentration of energy at the corresponding dam corner. Diffraction occurred at the opposite side of the wave tank with lateral spread of the wave energy. The solitary wave impact on the gravity and arch dam, respectively, for asymmetrical wave impact, are shown in Fig. 19.

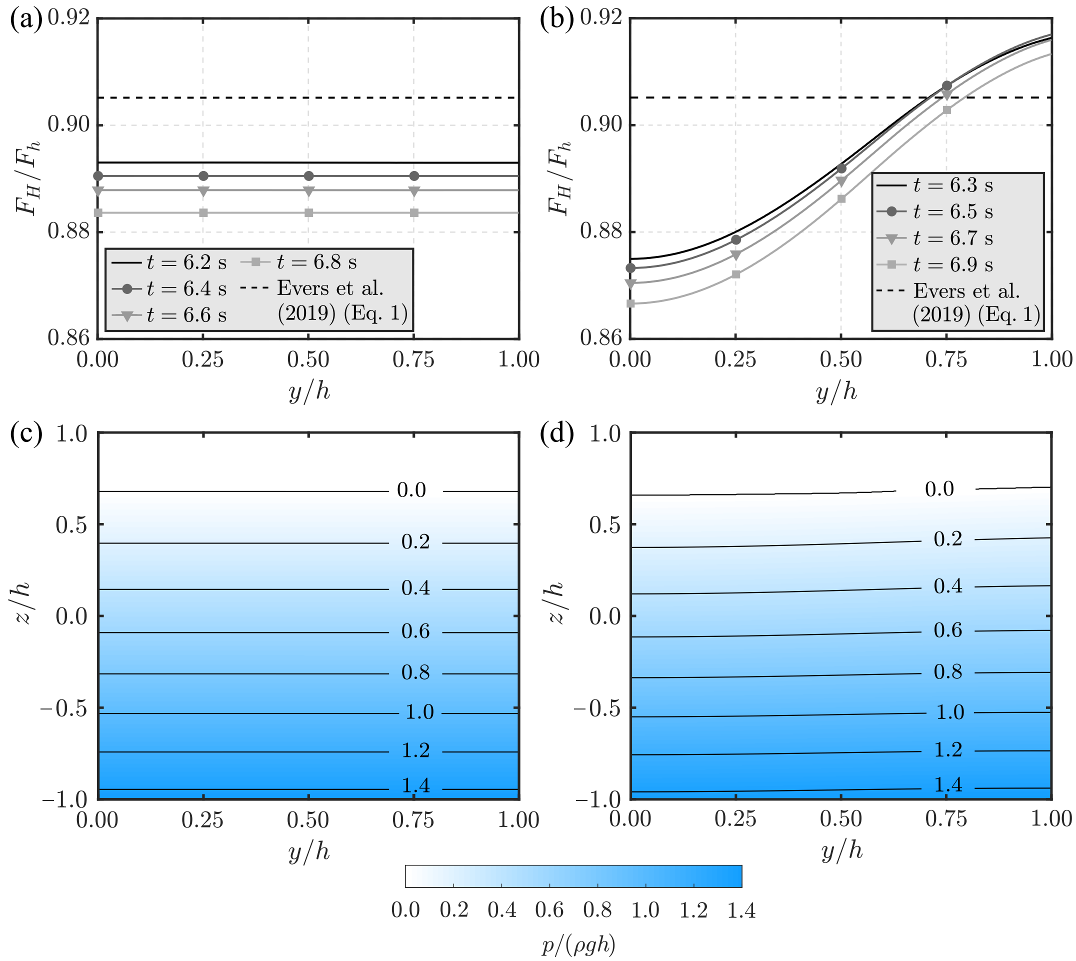


**Fig. 17.** Symmetrical wave impact ($\gamma = 0°$): dimensionless force $F_H/F_h$ versus the relative dam width $y/h$ at the (a) gravity and (b) arch dam and pressure $p/(\rho g h)$ versus $y/h$ and $z/h$ during the maximum force at the (c) gravity and (d) arch dam.

The concentration of energy at the dam flank at $y/h = -1$, resulted in a significant increase of $R/h$ for both the gravity and arch dam. For the gravity dam, $R/h$ overall increases across the dam width (Fig. 19a,b,c). For $t \geq 2.5$ s, $R/h$ is approximately constant at $-1.00 \leq y/h \leq -0.75$, reaching the maximum $R/h = 0.82$ at $t = 3.0$ s. This is 64 and 21% larger compared to the maximum $R/h$ at $y/h = 1$ and the prediction with Eq. (13), respectively. The effect of the asymmetrical wave impact is even more relevant in combination with the effect of the curvature of the dam. As revealed by Fig. 19d,e,f, $R/h$ reaches the maximum of 0.90 at $y/h = -1$ and $t = 4.0$ s for the arch dam, which is 32% larger than the prediction with Eq. (13). The maximum $R/h = 0.55$ at $y/h = 1$ occurs at $t = 3.0$ s and is 63% smaller than at $y/h = -1$.

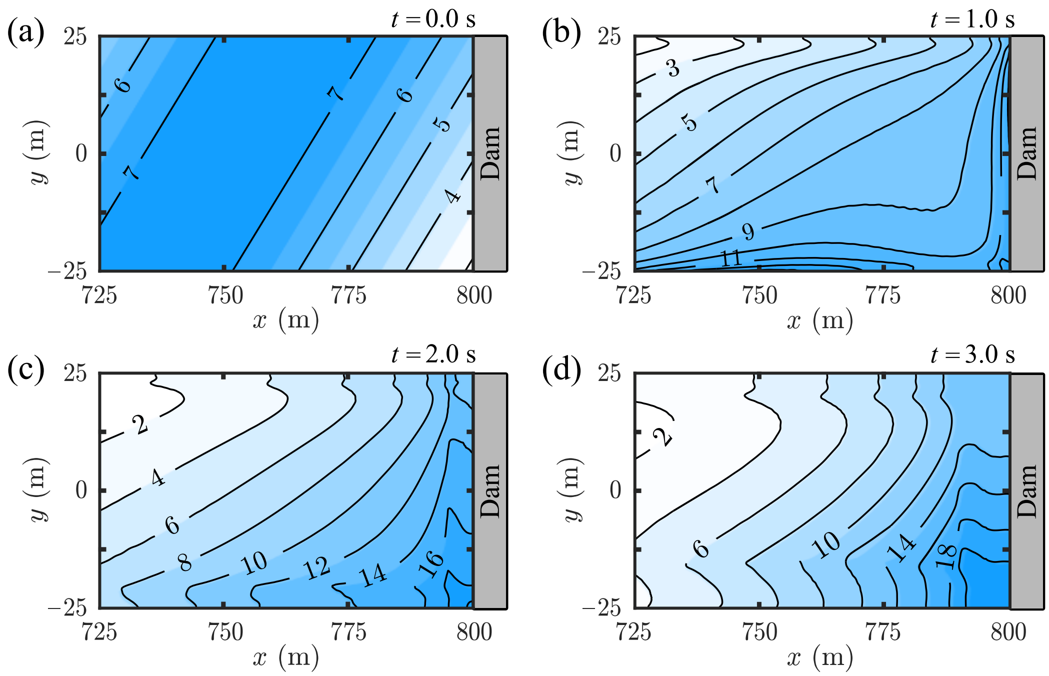


**Fig. 18.** Snapshot series with surface elevation contours in m of a solitary wave impact on the gravity dam with $a/h = 0.3$ and $\gamma = 30°$ at $t =$ (a) 0.0, (b) 1.0, (c) 2.0, and (d) 3.0 s.

Fig. 20a,b shows $F_H/F_h$ versus $y/h$ for the gravity and arch dams. $F_H/F_h$ increases with smaller $y/h$ for the gravity dam, reaching a maximum of 0.91 at $y/h = -1$. $F_H/F_h$ is approximately constant for the arch dam at $0.6 < y/h \leq 1.0$, decreases for $0.3 \leq y/h \leq 0.6$ and increases for $y/h < 0.3$, reaching the maximum $F_H/F_h = 0.97$ at $y/h = -1$. The gravity and arch dams show similar values of $F_H/F_h$ for $y/h > 0.6$, while the curvature of the arch dam induces larger $F_H/F_h$ in proximity of the flank at $y/h = -1$. Although $F_H$ may not be normal to the dam axis, due to $\gamma \neq 0°$ and the curvature of the dam, the maximum $F_H/F_h$ is once more well predicted by Eq. (1) for both the gravity and arch dams, with small underestimations of a maximum of 7%. The maximum $F_{H,3D}/(bF_h)$ resulted in 0.87 and 0.88 and the contours of $p$ at $t$ during the maximum $F_{3D}$ are shown in Fig. 20c,d.

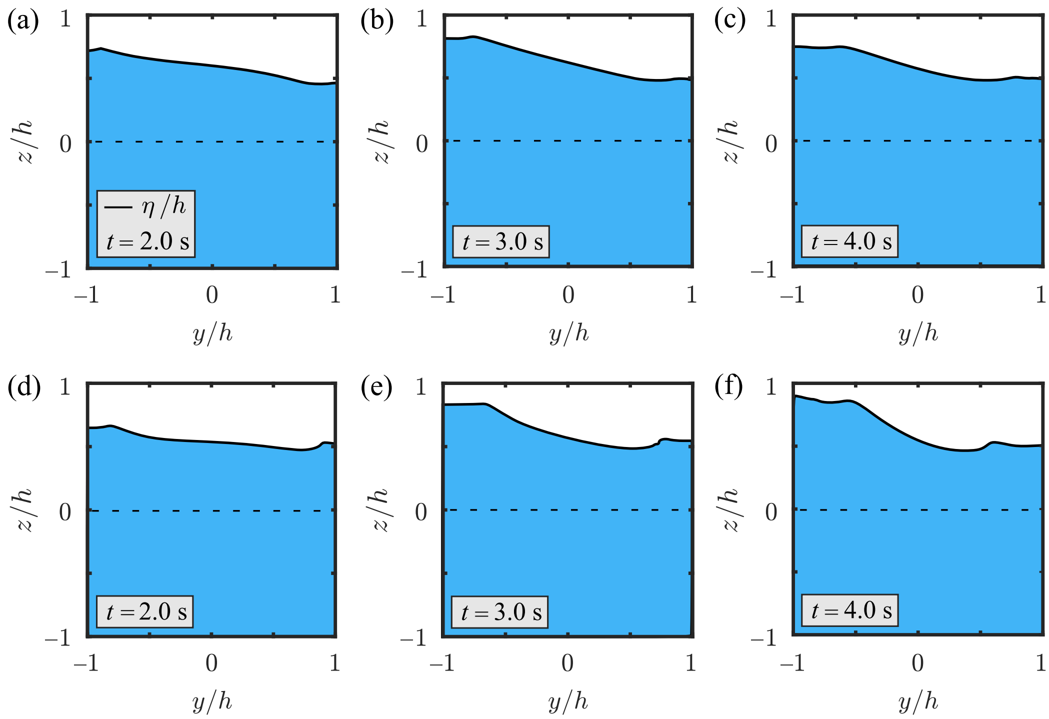


**Fig. 19.** Snapshot series of a solitary wave impact on the (a,b,c) gravity and (d,e,f) arch dams with $a/h = 0.3$ and $\gamma = 30°$ at $t = 2, 3,$ and 4 s.

As discussed above, the boundaries of the reservoir confine the tsunami with a significant concentration of energy in proximity of the dam. The dam curvature and asymmetrical wave impact resulted both in higher $R$ at the dam flanks. These two effects combined resulted in an increase of $R$ of up to 32%. In contrast, these 3D effects can be neglected for $F_H$. Although in nature some reservoirs have a similar geometry as the one investigated in the present study, e.g. the Derwent reservoir in England and the Luzzone reservoir in Switzerland, in most cases, the reservoir geometry is less idealised. Furthermore, the waves may approach the dam with a more extreme angle than $\gamma = 30°$ and the bathymetry may not be flat. Therefore, the wave behaviour can be more complex (Couston et al., 2015; Ruffini et al., 2019).

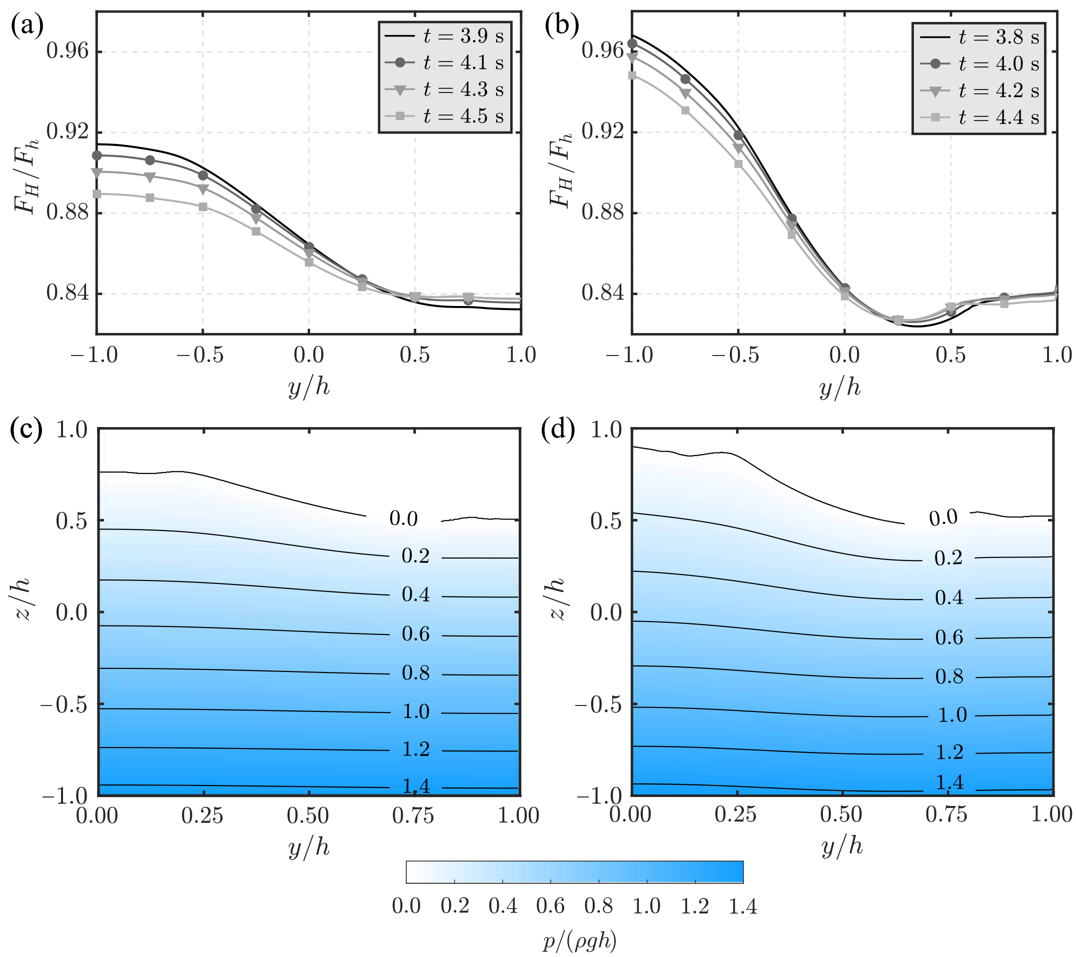


**Fig. 20.** Asymmetrical wave impact ($\gamma = 30°$): dimensionless force $F_H/F_h$ versus the relative dam width $y/h$ at the (a) gravity and (b) arch dam and pressure $p/(\rho g h)$ versus $y/h$ and $z/h$ during the maximum force at the (c) gravity and (d) arch dam.

## 5. Conclusions

The present article aimed to investigate landslide-tsunamis impacting dams with the numerical toolbox solids4foam in foam-extend. This investigation was motivated by the limited validation of available prediction methods for tsunami pressures and forces on dams, which is also a drawback for a range of offshore and coastal engineering applications. Moreover, additional methods to predict the overtopping waves under certain conditions were required.

The numerical toolbox solids4foam was successfully validated with available laboratory measurements, an analytical model, and a numerical solution for pressures, forces, and overtoppings of waves impacting a vertical wall. A total of 72 2D numerical experiments with 5th order Stokes, cnoidal, and solitary waves impacting dams of inclinations $60° \leq \beta \leq 90°$ were performed. The tsunami forces and moments on dams were in agreement with predictions based on Evers et al. (2019), extending their validation ranges.

New empirical equations for the wave run-up heights $R$, overtopping volumes $\cancel{V}$, and maximum depths over the dam $d_0$ were proposed. $R$ was expressed in function of the wave amplitude relative to the water depth $a/h$ and $\beta$ (Eq. 13). $\cancel{V}$ and $d_0$ were expressed in function of $a$, $h$, $f$, and $\beta$ (Eqs. 23 and 24) for the tests with $a \leq f$. Larger waves resulted in larger $\cancel{V}$ and $d_0$. In contrast, $\cancel{V}$ and $d_0$ decreased with increasing freeboard $f$ for a given wave (Fig. 13). A summary of the most suitable equations to predict $R$, $\cancel{V}$, and $d_0$ is shown in Table 5. Further, a new semi-empirical approach for the dynamic pressure of tsunamis impacting dams was presented in Section 3.2.3. This approach, combined with the prediction of the total pressure from Evers et al. (2019), provides the dynamic component of the pressure.

Furthermore, a total of 4 3D simulations were conducted with either a straight or an arch dam impacted by solitary waves normal or at an angle of 30° (Section 4.4). For a normal wave impact, the curvature of the dam induced larger $R$ at the dam flanks of up to 9%, while the effects on the force can be neglected such that the 2D equations of Evers et al. (2019) apply. For a solitary wave with asymmetrical wave impact of 30°, $R$ was 21 and 32% larger for the gravity and arch dam, respectively, compared to the prediction for normal wave impact.

Future work will focus on waves interacting with flexible structures. The effects of the structural deformation on the wave field will be investigated together with scale effects for both rigid and flexible structures.

## Declaration of competing interest

The authors declare that they have no known competing financial interests or personal relationships that could have appeared to influence the work reported in this paper.

## Acknowledgements

The authors would like to thank Dr. Frederic Evers from the Laboratory of Hydraulics, Hydrology and Glaciology, ETH Zurich, for providing the experimental data of Kobel et al. (2017) and the photos in Fig. 4. The PhD study of Tommaso Attili is financially supported by the Vice-Chancellor's Scholarship for Research Excellence. The simulations were conducted on the HPC cluster Augusta at the University of Nottingham.

## Appendix A. Overtopping wave forces at dams

Waves overtop a dam when the run-up height $R$ exceeds the freeboard $f$. For $f < 2a$, Evers et al. (2019) followed Heller et al. (2009) by suggesting a reduction of the force effects due to hydrostatic and wave pressures by removing the triangular section of the pressure above the dam crest (Fig. 3.11b in Evers et al., 2019). This results in a trapezoidal distribution of the pressure and the reduced horizontal force per unit dam width is

$$F_{H,red} = \frac{(h+f)}{2}\left[p_K + \frac{2F_H}{2a+h}\right]. \tag{A.1}$$

In Eq. (A.1) $F_H$ is the force that would act on the dam without overtopping (Eq. 1) and $p_k$ is the pressure at the dam crest

$$p_K = \frac{2F_H}{(2a+h)^2}(2a-f). \tag{A.2}$$

## Appendix B. Convergence tests

### *Appendix B.1. Convergence of the main tests*

The numerical set-up used for the main tests and its discretisation is presented in Section 2.2. Convergence tests with a solitary wave of $a/h = 0.31$ have been conducted to find the optimal cell sizes. Resolutions of $\Delta x = \Delta z =$ 50.000, 25.000, 12.500, 6.250, and 3.125 cm have been investigated. The finest resolutions $\Delta x = \Delta z =$ 12.500, 6.250, and 3.125 cm were applied in a 25 m $\times$ 80 m area in front of the dam and $\Delta x = \Delta z =$ 25.000 cm was used in the rest of the domain (Fig. 1a). The convergence is shown here in terms of the force

$$F(t) = \sum\nolimits_{\mathrm{i}}^{\mathrm{N}} \frac{p(z_{\mathrm{i}},t) + p(z_{\mathrm{i}+1},t)}{2}\Delta z, \tag{B.1}$$

with $p(z_{\mathrm{i}}, t)$ as the numerical pressure at a certain height $z$ and N as the number of $p(z)$ values. The maximum $F/(\rho g h^2/2)$ versus $\Delta x$ ($= \Delta z$) is shown in Fig. B.1a.

The values of $F/(\rho g h^2/2)$ increase with decreasing cell sizes and the deviations between each $\Delta x$ and $\Delta x/2$ decrease for smaller $\Delta x$ (Fig. B.1a). $\Delta x = \Delta z =$ 6.250 cm was used for the main tests as convergence is achieved, resulting only in a 0.18% smaller value for $F/(\rho g h^2/2)$ than for $\Delta x = \Delta z =$ 3.125 cm and requiring only 1/6 of the computation time.

*Appendix B.2. Convergence of the validation tests*

The numerical set-up for the validation tests in Section 3.1.1 has the same geometry as the experimental set-up of Mallayachari and Sundar (1995). The domain was discretised with squared cells and mesh resolutions of $\Delta x = \Delta z = 6.00$, 3.00, 1.50, and 0.75 mm were investigated. The last two were applied only in a $L/4 \times 0.630$ m area in front of the plate and $\Delta x = \Delta z = 3.00$ mm was used in the rest of the domain.

Convergence tests were performed for the experiment shown in Fig. 2a. $F$ on the plate is shown in Fig. B.1b in function of the mesh sizes. Considering the small increment of $F/(\rho g h^2/2)$ of 1.4% between $\Delta x = \Delta z = 1.50$ and 0.75 mm (Fig. B.1b), the larger computational efforts and some instability issues which occurred for $\Delta x = \Delta z = 0.75$ mm, $\Delta x = \Delta z = 1.50$ mm resulted in the optimal resolution.

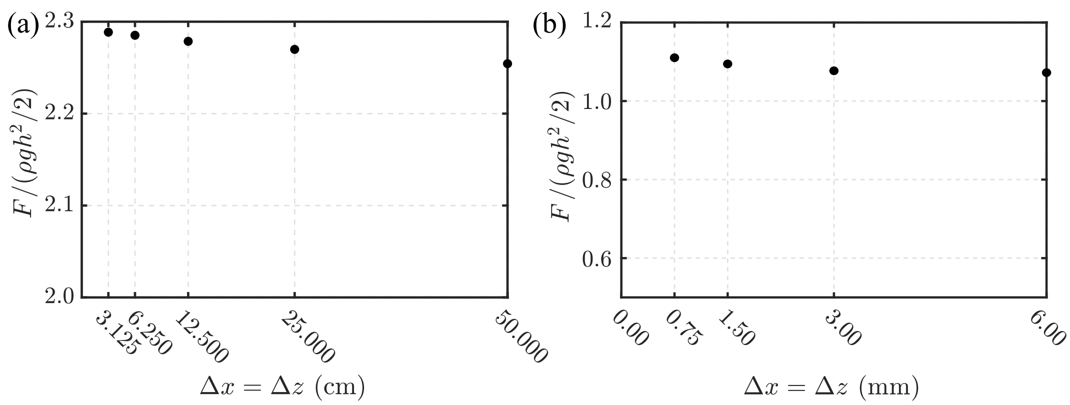


**Fig. B.1.** Convergence tests of the relative force $F/(\rho g h^2/2)$ with the mesh size $\Delta x = \Delta z$ for the (a) main and (b) validation tests.

## Appendix C. Overtopping waves: dynamic pressure

The dynamics of the overtopping water may have a significant effect on $p_d$ due to the additional water depth and larger velocities $u_x(z)$ in proximity of the crest compared to the waves which do not overtop. Fig. C.1a,b shows the distribution of $p$ and $p_d$ in 2 solitary wave tests with $a/h = 0.21$, at $h = 36$ and 48 m, respectively. Due to the larger $f/h$ of the test in Fig. C.1a compared to Fig. C.1b, smaller values of $p$ were observed in proximity of the dam crest. In other words, a larger $d_0$ was observed in Fig. C.1b, resulting in a larger $p$ at the dam crest compared to Fig. C.1a.

For the Stokes and cnoidal wave tests, with $0.07 \leq a/h \leq 0.08$ and $f/h = 0.042$, $K_{pw}$ is poorly captured by Eq. (20) with $nRMSE$ of up to 3.13 (Fig. C.1c). For the solitary wave tests with $0.21 \leq a/h \leq 0.44$ and $0.389 \leq f/h \leq 1.000$, the overtopping dynamics does not modify the pressure field significantly. In these cases, $K_{pw}$ is captured by Eq. (21) with $nRMSE =$ 0.06 to 0.41 for most tests apart from two with 0.79 and 1.86. For larger values of $a/h$ and/or smaller $f/h$ a different trend of $K_{pw}(z)$ is observed. In these cases, $K_{pw}$ is larger then 1, reaches a peak in proximity of $z/h = -0.20$ and decreases then, as shown in Fig. C.1d for some representative tests. This trend is likely due to the larger $d_0$ compared to the cases with smaller $a/h$ and/or larger $f/h$.

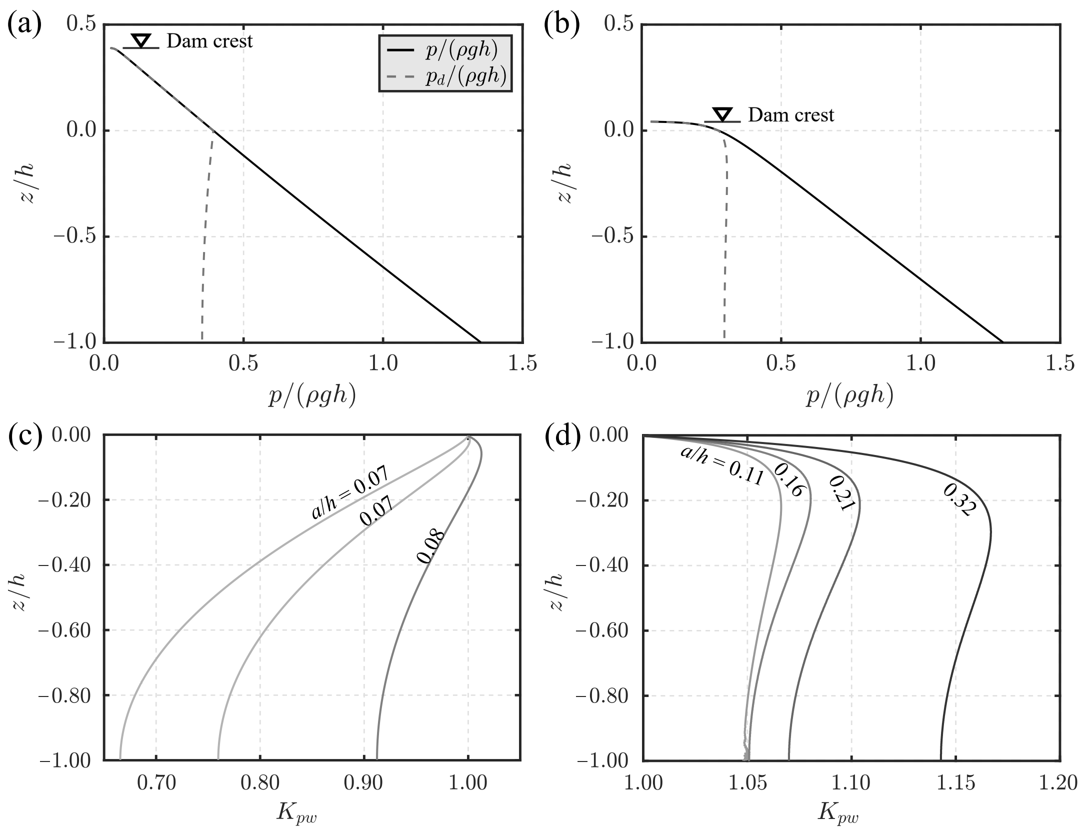


**Fig. C.1.** Total pressure $p$ and dynamic pressure $p_d$ at the dam in two overtopping tests with $a/h = 0.21$ and $\beta = 90°$ with (a) $f/h = 0.389$ and (b) $f/h = 0.042$ and pressure response factor at the wall $K_{pw}$ versus $z/h$ for $f/h = 0.042$ for some representative (c) cnoidal and (d) solitary wave overtopping tests for $\beta = 90°$.

The pressure $p(z)$ can be approximated with the trapezoidal distribution proposed by Evers et al. (2019) (Appendix A) for engineering applications with wave overtoppings. For $0.21 \leq a/h \leq 0.44$ and $0.389 \leq f/h \leq 1.000$, the component $p_d$ can be predicted as for waves without overtopping (Eq. 16) with $K_{pw}$ defined in Eq. (21). For larger $a/h$ and/or smaller $f/h$, it is challenging to find an expression for $K_{pw}(z)$ (Fig. C.1c,d). However, a good preliminary estimation of $p_d$ can be achieved in these cases by subtracting the hydrostatic component of the pressure from $p(z)$ (Eq. 11).

# Notation

| | |
|---|---|
| $A$ | Coefficient of the pressure response factor at the wall |
| $a$ | Wave amplitude, m |
| $b$ | Dam width, m |
| $C$ | Courant number |
| $d_0$ | Maximum wave overtopping depth, m |
| $\mathbf{F}$ | Force vector on dam per unit width resulting from a tsunami and hydrostatic pressure, N/m |
| $\mathbf{F}_{3D}$ | Force vector on dam resulting from a tsunami and hydrostatic pressure, N |
| $F$ | Force on dam per unit width resulting from a tsunami and hydrostatic pressure, N/m |
| $F_h$ | Hydrostatic force per unit width due to still water, N/m |
| $f$ | Freeboard, m |
| $\mathbf{g}$ | Gravitational acceleration vector, m/s$^2$ |
| $g$ | Gravitational acceleration, m/s$^2$ |
| $H$ | Wave height, m |
| $h$ | Water depth, m |
| I | Identity matrix |
| $K_p$ | Pressure response factor |
| $k$ | Wave number, 1/m |
| $k_t$ | Turbulent kinetic energy per unit mass, m$^2$/s$^2$ |
| $L$ | Wave length, m |
| $l$ | Dam height, m |
| $M_h$ | Bending moment per unit width relative to the foundation due to the hydrostatic pressure, Nm/m |
| N, P | Numbers of the considered pressure values |
| $\mathrm{N_d}$ | Number of the considered dynamic pressure values |
| $\mathbf{n}$ | Normal vector to the dam surface |
| $nRMSE$ | Normalised Root Mean Square Error |
| $p$ | Total pressure, N/m$^2$ |
| $\bar{p}$ | Mean total pressure, N/m$^2$ |
| $p_d$ | Dynamic pressure, N/m$^2$ |
| $p_k$ | Pressure at the dam crest resulting from a tsunami and hydrostatic pressure with overtopping, N/m$^2$ |
| $p_{lin}$ | Linear dynamic wave pressure of Tadjbakhsh and Keller (1960), N/m$^2$ |
| $p_{nonlin}$ | Nonlinear dynamic wave pressure of Tadjbakhsh and Keller (1960), N/m$^2$ |

| | |
|---|---|
| $q$ | Discharge per unit dam width, $m^2/s$ |
| $R$ | Wave run-up height, m |
| $R^2$ | Coefficient of determination |
| $S$ | Cell area, $m^2$ |
| $s$ | Dam thickness, m |
| $T$ | Wave period, s |
| $t$ | Time, s |
| $t_0$ | Instant during the maximum run-up, s |
| $t_{d0}$ | Instant during the maximum wave overtopping depth, s |
| $\bar{\mathbf{u}}$ | Mean fluid velocity vector, m/s |
| $\overline{\mathbf{u}'\mathbf{u}'}$ | Turbulent stress tensor, $N/m^2$ |
| $\mathbf{u_r}$ | Compression velocity vector, m/s |
| $\bar{u}$ | Mean fluid velocity, m/s |
| $\bar{u}_x, \bar{u}_y, \bar{u}_z$ | Mean fluid velocity component along $x$-, $y$-, $z$-axis, m/s |
| $\cancel{V}$ | Overtopping volume per unit dam width, $m^3/m$ |
| $x, y, z$ | $x$-, $y$-, $z$-axis, m |
| $\bar{y}$ | Mean of the numerical values |
| $z_H$ | Elevation of the resultant of $F_H$ from the dam foundation, m |
| $\alpha$ | Fraction of volume |
| $\beta$ | Dam inclination, $^\circ$ |
| $\gamma$ | Wave propagation angle, $^\circ$ |
| $\Delta d_0$ | Deviation between the experimental and numerical maximum wave overtopping depth, % |
| $\Delta t$ | Time step, s |
| $\Delta \cancel{V}$ | Deviation between the experimental and numerical overtopping volume per unit dam width, % |
| $\Delta x, \Delta y, \Delta z$ | Cell sizes, m |
| $\eta$ | Water surface elevation, m |
| $\mu$ | Fluid dynamic viscosity, $Ns/m^2$ |
| $\nu_t$ | Kinematic turbulent viscosity, $m^2/s$ |
| $\rho$ | Fluid density, $kg/m^3$ |
| $\tau$ | Adjusted time, s |

## Subscripts

| | |
|---|---|
| $a$ | Air |
| $exp$ | Experimental |

| | |
|---|---|
| $H$ | Horizontal |
| $max$ | Maximum |
| $min$ | Minimum |
| $num$ | Numerical |
| $pred$ | Predicted |
| $red$ | Reduced |
| $ref$ | Reference solution |
| $w$ | Wall, water |

## Abbreviations

| | |
|---|---|
| CFD | Computational Fluid Dynamics |
| CFL | Courant-Friedrichs-Lewy |
| CPU | Central Processing Unit |
| FE 4.0 | Foam-Extend 4.0 |
| FVM | Finite Volume Method |
| PIMPLE | Combination of Pressure Implicit Splitting Operator (PISO) and Semi-Implicit Method for Pressure-Linked Equations (SIMPLE) |
| RANS | Reynolds-Averaged Navier–Stokes |
| SPH | Smoothed Particle Hydrodynamics |
| VOF | Volume Of Fluid |
| 2D | Two-dimensional (channel) |
| 3D | Three-dimensional (basin) |

## References


Aguerre, H. J., Damián, S. M., Gimenez, J. M., Nigro, N. M., 2013. Modeling of compressible fluid problems with OpenFOAM using dynamic mesh technology. Mecánica Computacional 32 (13), 995 – 1011.

Attili, T., Heller, V., Triantafyllou, S., 2020. Numerical modelling of impulse wave forces on dams. Proceedings of the 1st IAHR Young Professionals Congress online, 17-18 November 2020, 186 – 187.

Boussinesq, J., 1871. Théorie de l'intumescence liquide appelée onde solitaire ou de translation, se propageant dans un canal rectangulaire. Comptes Rendus de l'Académie des Science 72, 755 – 759.

Bredmose, H., Bullock, G., Hogg, A., 2015. Violent breaking wave impacts. Part 3. Effects of scale and aeration. Journal of Fluid Mechanics 765, 82 – 113.

Bullard, G., Mulligan, R., Carreira, A., Take, W., 2019. Experimental analysis of tsunamis generated by the impact of landslides with high mobility. Coastal Engineering 152, 103538.

Bureau of Reclamation, 2012. Embankment dams. URL: https://www.usbr.gov/tsc/techreferences/designstandards-datacollectionguides/finalds-pdfs/DS13-6.pdf, accessed: 1 June 2021.

Bureau of Reclamation, 2013. Design of double-curvature arch dams planning, appraisal, feasibility level. Technical Memorandum EM36-86-68110.

Cardiff, P., Karač, A., Jaeger, P. D., Jasak, H., Nagy, J., Ivanković, A., Tuković, Z., 2018. An open-source finite volume toolbox for solid mechanics and fluid-solid interaction simulations. ArXiv Prepr ArXiv180810736.

Castellino, M., Romano, A., Lara, J. L., Losada, I. J., De Girolamo, P., 2021. Confined-crest impact: forces dimensional analysis and extension of the Goda's formulae to recurved parapets. Coastal Engineering 163, 103814.

Castellino, M., Sammarco, P., Romano, A., Martinelli, L., Ruol, P., Franco, L., De Girolamo, P., 2018. Large impulsive forces on recurved parapets under non-breaking waves. A numerical study. Coastal Engineering 136, 1 – 15.

Chen, F., Heller, V., Briganti, R., 2020. Numerical modelling of tsunamis generated by iceberg calving validated with large-scale laboratory experiments. Advances in Water Resources, 103647.

Chen, L., Zang, J., Hillis, A., Morgan, G., Plummer, A., 2014. Numerical investigation of wave–structure interaction using OpenFOAM. Ocean Engineering 88, 91 – 109.

Cooker, M. J., Weidman, P. D., Bale, D. S., 1997. Reflection of a high-amplitude solitary wave at a vertical wall. Journal of Fluid Mechanics 342, 141 – 158.

Courant, R., Friedrichs, K., Lewy, H., 1928. Über die partiellen Differenzengleichungen der Mathematischen Physik. Mathematische Annalen 100, 32 – 74.

Couston, L.-A., Mei, C., Alam, M.-R., 2015. Landslide tsunamis in lakes. Journal of Fluid Mechanics 772, 784 – 804.

Dean, R., Dalrymple, R., 1991. Water wave mechanics for engineers and scientists. Advanced series on ocean engineering 2. World Scientific, Singapore.

Dermentzoglou, D., Castellino, M., De Girolamo, P., Partovi, M., Schreppers, G.-J., Antonini, A., 2021. Crownwall failure analysis through finite element method. Journal of Marine Science and Engineering 9 (1), 35.

Di Paolo, B., Lara, J. L., Barajas, G., Íñigo J. Losada, 2021. Wave and structure interaction using multi-domain couplings for Navier-Stokes solvers in OpenFOAM®. Part I: implementation and validation. Coastal Engineering 164, 103799.

Didier, E., Neves, D., Martins, R., Neves, M., 2014. Wave interaction with a vertical wall: SPH numerical and experimental modeling. Ocean Engineering 88, 330 – 341.

Dingemans, M. W., 1997. Water wave propagation over uneven bottoms. Advanced Series on Ocean Engineering.

Evers, F. M., 2017. Spatial propagation of landslide generated impulse waves. Phd thesis no. 24650, ETH Zurich, Zurich.

Evers, F. M., Boes, R. M., 2019. Impulse wave runup on steep to vertical slopes. Journal of Marine Science and Engineering 7 (1), 8.

Evers, F. M., Heller, V., Hager, W. H., Boes, R. M., 2019. Landslide-generated impulse waves in reservoirs: basics and computation. 2nd edition. VAW-Mitteilung 254 (R. Boes, ed.), ETH Zurich, Zurich.

Fenton, J. D., Rienecker, M. M., 1982. A Fourier method for solving nonlinear water-wave problems: application to solitary-wave interactions. Journal of Fluid Mechanics 118, 411 – 443.

Ferziger, J. H., 1987. Simulation of incompressible turbulent flows. Journal of Computational Physics 69 (1), 1 – 48.

Franci, A., Cremonesi, M., Perego, U., Crosta, G., Oñate, E., 2020. 3D simulation of Vajont disaster. Part 1: numerical formulation and validation. Engineering Geology 279, 105854.

Galvin, C. J., 1968. Breaker type classification on three laboratory beaches. Journal of Geophysical Research 73 (12), 3651 – 3659.

Gylfadóttir, S. S., Kim, J., Helgason, J. K., Brynjólfsson, S., Höskuldsson, A., Jóhannesson, T., Harbitz, C. B., Løvholt, F., 2017. The 2014 lake Askja rockslide-induced tsunami: optimization of numerical tsunami model using observed data. Journal of Geophysical Research: Oceans 122 (5), 4110 – 4122.

Hall, J. V., Watts, G. M., 1953. Laboratory investigation of the vertical rise of solitary waves on impermeable slopes. Technical Memo Report No. 33; U.S. Army Corps of Engineers, Beach Erosion Board: Washington, DC, USA.

He, G., Kashiwagi, M., 2012. Numerical analysis of the hydroelastic behavior of a vertical plate due to solitary waves. Journal of Marine Science and Technology 17 (2), 154 – 167.

Heller, V., 2011. Scale effects in physical hydraulic engineering models. Journal of Hydraulic Research 49 (3), 293 – 306.

Heller, V., Attili, T., Chen, F., Gabl, R., Wolters, G., 2021. Large-scale investigation into iceberg-tsunamis generated by various iceberg calving mechanisms. Coastal Engineering 163, 103745.

Heller, V., Bruggemann, M., Spinneken, J., Rogers, B. D., 2016. Composite modelling of subaerial landslide–tsunamis in different water body geometries and novel insight into slide and wave kinematics. Coastal Engineering 109, 20 – 41.

Heller, V., Hager, W. H., 2010. Impulse product parameter in landslide generated impulse waves. Journal of Waterway, Port, Coastal, and Ocean Engineering 136 (3), 145 – 155.

Heller, V., Hager, W. H., 2011. Wave types of landslide generated impulse waves. Ocean Engineering 38 (4), 630 – 640.

Heller, V., Hager, W. H., Minor, H.-E., 2009. Landslide-generated impulse waves in reservoirs: basics and computation. VAW-Mitteilung 211 (R. Boes, ed.), ETH Zurich, Zurich.

Heller, V., Spinneken, J., 2015. On the effect of the water body geometry on landslide–tsunamis: physical insight from laboratory tests and 2D to 3D wave parameter transformation. Coastal Engineering 104, 113 – 134.

Hirt, C. W., Nichols, B. D., 1981. Volume of fluid (VOF) method for the dynamics of free boundaries. Journal of Computational Physics 39, 201 – 225.

Hu, Z. Z., Greaves, D., Raby, A., 2016. Numerical wave tank study of extreme waves and wave-structure interaction using OpenFOAM. Ocean Engineering 126, 329 – 342.

Jacobsen, N. G., Fuhrman, D. R., Fredsøe, J., 2012. A wave generation toolbox for the open-source CFD library: OpenFOAM. International Journal for Numerical Methods in Fluids 70 (9), 1073 – 1088.

Jasak, H., 1996. Error analysis and estimation for the finite volume method with applications to fluid flows. Phd thesis, Imperial College of Science, Technology and Medicine, London.

Kobel, J., Evers, F. M., Hager, W. H., 2017. Impulse wave overtopping at rigid dam structures. Journal of Hydraulic Engineering 143 (6), 04017002.

Le Méhauté, B., 1976. An introduction to hydrodynamics and water waves. Springer, New York.

Lo, H.-Y., Park, Y. S., Liu, P. L.-F., 2013. On the run-up and back-wash processes of single and double solitary waves - an experimental study. Coastal Engineering 80, 1 – 14.

Mallayachari, V., Sundar, V., 1995. Standing wave pressures due to regular and random waves on a vertical wall. Ocean Engineering 22 (8), 859 – 879.

Martinelli, L., Ruol, P., Volpato, M., Favaretto, C., Castellino, M., De Girolamo, P., Franco, L., Romano, A., Sammarco, P., 2018. Experimental investigation on non-breaking wave forces and overtopping at the recurved parapets of vertical breakwaters. Coastal Engineering 141, 52 – 67.

Maxworthy, T., 1976. Experiments on collisions between solitary waves. Journal of Fluid Mechanics 76 (1), 177–186.

Meng, Z., Hu, Y., Ancey, C., 2020. Using a data driven approach to predict waves generated by gravity driven mass flows. Water 12 (2), 600.

Müller, D. R., 1995. Auflaufen und Überschwappen von Impulswellen an Talsperren. Phd thesis no. 24650, ETH Zurich.

Mulligan, R. P., Franci, A., Celigueta, M. A., Take, W. A., 2020. Simulations of landslide wave generation and propagation using the particle finite element method. Journal of Geophysical Research: Oceans 125 (6), e2019JC015873.

OpenFOAM documentation, 2020. User guide. URL: https://openfoam.com/documentation/user-guide/, accessed: 1 June 2021.

OpenFOAM extension, 2016. URL: https://sourceforge.net/u/hjasak/foam-extend-4.0/ci/master/tree/, accessed: 1 June 2021.

Panizzo, A., De Girolamo, P., Di Risio, M., Maistri, A., Petaccia, A., 2005a. Great landslide events in Italian artificial reservoirs. Natural Hazards and Earth System Science 5 (5), 733 – 740.

Panizzo, A., De Girolamo, P., Petaccia, A., 2005b. Forecasting impulse waves generated by subaerial landslides. Journal of Geophysical Research: Oceans 110 (C12), 1 – 23.

Ramsden, J. D., 1996. Forces on a vertical wall due to long waves, bores, and dry-bed surges. Journal of Waterway, Port, Coastal, and Ocean Engineering 122 (3), 134 – 141.

Rauter, M., Hoße, L., Mulligan, R., Take, W., Løvholt, F., 2021. Numerical simulation of impulse wave generation by idealized landslides with OpenFOAM. Coastal Engineering 165, 103815.

Romano, A., Lara, J., Barajas, G., Di Paolo, B., Bellotti, G., Di Risio, M., Losada, I., De Girolamo, P., 2020. Tsunamis generated by submerged landslides: numerical analysis of the near-field wave characteristics. Journal of Geophysical Research: Oceans 125 (7), e2020JC016157.

Ruffini, G., Heller, V., Briganti, R., 2019. Numerical modelling of landslide-tsunami propagation in a wide range of idealised water body geometries. Coastal Engineering 153, 103518.

Ruffini, G., Heller, V., Briganti, R., 2021. Numerical characterisation and efficient prediction of landslide-tsunami propagation over a wide range of idealised bathymetries. Coastal Engineering, 103854.

Sainflou, M., 1928. Essai sur les digues maritimes verticales (test on vertical sea dikes). Annales des Ponts et Chaussees 98, 5 – 48.

Street, R. L., Camfield, F. E., 1967. Observations and experiments on solitary wave deformation. In: Coastal Engineering 1966. pp. 284–301.

Streeter, V. L., Wylie, E. B., 1985. Fluid Mechanics. McGraw-Hill, New York.

Swiss Federal Office of Energy, 2015. Directive on the Safety of Water Retaining Facilities. Swiss Federal Office of Energy, Supervision of Dams Section, Bern.

Tadjbakhsh, I., Keller, J., 1960. Standing surface waves of finite amplitude. Journal of Fluid Mechanics 8 (3), 442 – 451.

Teng, M. H., Feng, K., Liao, T. I., 2000. Experimental study on long wave run-up on plane beaches. In Proceedings of the 10th International Offshore and Polar Engineering Conference, Seattle, WA, USA, 28 May–2 June 2000; The International Society of Offshore and Polar Engineers ISOPE-I-00-310, 660 – 664.

Tuković, Z., Karač, A., Cardiff, P., Jasak, H., Ivanković, A., 2018. OpenFOAM finite volume solver for fluid-solid interaction. Transactions of FAMENA 42, 1 – 31.

Wang, J., Ward, S. N., Xiao, L., 2015. Numerical simulation of the December 4, 2007 landslide-generated tsunami in Chehalis lake, Canada. Geophysical Journal International 201 (1), 372 – 376.

Watt, S. F., Pyle, D. M., Naranjo, J. A., Mather, T. A., 2009. Landslide and tsunami hazard at Yate volcano, Chile as an example of edifice destruction on strike-slip fault zones. Bulletin of Volcanology 71 (5), 559.

Weller, H., Tabor, G., Jasak, H., Fureby, C., 1998. A tensorial approach to computational continuum mechanics using object orientated techniques. Computers in Physics 12, 620 – 631.

Xue, H., Ma, Q., Diao, M., Jiang, L., 2019. Propagation characteristics of subaerial landslide-generated impulse waves. Environmental Fluid Mechanics 19 (1), 203 – 230.

Yavari-Ramshe, S., Ataie-Ashtiani, B., 2016. Numerical modeling of subaerial and submarine landslide-generated tsunami waves—recent advances and future challenges. Landslides 13 (6), 1325 – 1368.